

# LES of Low to High Turbulent Combustion in an Elevated Pressure Environment

Roman Keppeler · Eike Tangermann · Usman Allaudin · Michael Pfitzner

Received: 29 November 2012 / Accepted: 14 November 2013 / Published online: 24 December 2013  
© Springer Science+Business Media Dordrecht 2013

**Abstract** A subgrid scale flame surface density combustion model for the Large Eddy Simulation (LES) of premixed combustion is derived and validated. The model is based on fractal characteristics of the flame surface, assuming a self similar wrinkling of the flame between smallest and largest wrinkling length scales. Experimental and direct numerical simulation databases as well as theoretical models are used to derive a model for the fractal parameters, namely the cut-off lengths and the fractal dimension suitable in the LES context. The combustion model is designed with the intent to simulate low as well as high Reynolds number premixed turbulent flame propagation and with a focus on correct scaling with pressure. The combustion model is validated by simulations of turbulent Bunsen flames with methane and propane fuel at pressure levels between 0.1 MPa and 2 MPa and at turbulence levels of  $0 < u'/s_L^0 < 11$ , conditions typical for spark ignition engines. The predicted turbulent flame speed is in a very good agreement with the experimental data and a smooth transition from resolved flame wrinkling to fully modelled, nearly subgrid-only wrinkling is realized. Evaluating the influence of mesh resolution shows a predicted mean flame surface and turbulent flame speed independent of mesh resolution for cases with 9–86 % resolved flame surface. Additional simulations of a highly turbulent jet flame at 0.1 MPa and 0.5 MPa and the comparison with experimental data in terms of flame shape, velocity field and turbulent fluctuations validates the model also at conditions typical for gas turbines.

**Keywords** Large Eddy Simulation · Turbulent and laminar premixed flames · High pressure · Fractal modelling

---

R. Keppeler (✉) · E. Tangermann · U. Allaudin · M. Pfitzner  
Institut für Thermodynamik, Universität der Bundeswehr München, Neubiberg, Germany  
e-mail: roman.keppeler@unibw.de

M. Pfitzner  
e-mail: michael.pfitzner@unibw.de

## Nomenclature

### Arabic

$A$	cross section area
$c$	reaction progress variable
$C_R$	reaction constant
$D$	fractal dimension
$D_u$	heat diffusivity of unburnt mixture
$Da$	Damköhler number
$F$	function for flame brush thickness
$h$	cell size
$I$	turbulent intensity
$k$	turbulent energy
$Ka$	Karlovitz number
$L$	edge length of control volume
$l_t$	integral length scale of turbulence
$l_G$	Gibson scale
$l_F$	laminar flame thickness
$LES_I Q_k$	index for LES quality
$Le$	Lewis number
$Ma$	Markstein number
$p$	pressure
$p_c$	PDF (RANS)
$p_c$	FDF (LES)
$Re$	Reynolds number
$s_t$	turbulent flame speed
$s_L^0$	unstretched laminar flame speed
$s_L$	stretched laminar flame speed
$S$	surface
$S_{ij}$	shear stress tensor
$Sc$	Schmidt number
$t$	time
$T$	temperature
$u'$	rms turbulent velocity
$u_i$	velocity components
$x_i$	spatial coordinates $i$
$z$	flame normal direction
$U$	bulk velocity at the inlet
$V$	volume

### Greek

$\alpha$	diffusivity
$\beta$	exponent
$\beta_{Zel}$	Zel'dovich number
$\delta_t$	turbulent flamebrush thickness
$\Delta$	filter size
$\Gamma$	efficiency function
$\epsilon$	cutoff length scale
$\epsilon_\Delta$	dissipation rate
$\varphi$	angle

$\Phi$	equivalence ratio
$\eta$	Kolmogorov length scale
$\kappa$	flame stretch rate
$\kappa_S$	flame strain rate
$\mu$	dynamic viscosity
$\nu$	kinematic viscosity
$\rho$	density
$\Sigma$	flame surface density
$\tau$	heat release parameter
$\xi$	normalized flame normal direction
$\Xi$	flame wrinkling factor
$\dot{\omega}_c$	turbulent reaction source term
$\Omega$	domain

#### Acronyms

BC	boundary condition
CFD	computational fluid dynamics
DNS	direct numerical simulation
FSD	flame surface density
KPP	Kolmogorov-Petrivski-Piskunov
LES	large eddy simulation
RANS	Reynolds averaged Navier-Stokes equation
TFC	turbulent flame speed closure
<>	averaging

#### Subscripts

b	burnt
c	chemical
$\Delta$	filter size as length scale
i	inner
ov	outer
OC	Obukhov-Corrsin
res	Resolved
SGS	sub grid scale
t	turbulent
tot	total
u	unburnt

## 1 Introduction

Turbulent premixed combustion is a complex process mainly due to the strong interaction of turbulence and chemical reaction and due to thin flames at large reaction rates. Even assuming a one step reaction the modelling of the interaction of the flame front with turbulent motions remains a considerable challenge. Large Eddy Simulation (LES) is considered to be a promising tool to investigate and simulate premixed turbulent combustion processes since it resolves the 3-dimensional and transient motion of the large eddies which exhibit geometry dependent structures and cause non universal unsteady motions [18]. Since only the more universal small structures need to be modelled, LES might be a promising approach towards a more universal combustion model. The use of LES is promoted by the rapidly increasing computational power and allows the simulation of complex and moderate Reynolds number

combustion cases and the simulation of a large number of operation points. The modelling of the turbulent reaction rate  $\dot{\omega}_c$  is the main challenge in turbulent premixed combustion modelling. A common approach is to utilize the flame surface density (FSD) or the flame wrinkling concept, respectively. The FSD  $\Sigma$ , representing in RANS the mean flame-surface area per control volume and in LES context the flame surface area within the filter volume is linked to the flame wrinkling factor  $\Xi$  via [58]:

$$\Sigma = \Xi \cdot |\nabla \bar{c}| \quad (1)$$

where  $\bar{c}$  describes the Reynolds average of the reaction progress  $c$  in the RANS context and its filtered value in LES. The FSD  $\Sigma$  or the flame wrinkling factor  $\Xi$  can be computed via transport equations or using an algebraic formulation, where an equilibrium of production and dissipation of  $\Sigma$  or  $\Xi$  is assumed. Transport equations provide a more general way to describe the evolution of  $\Sigma$  or  $\Xi$ , while algebraic models can be simpler, less expensive and numerically more robust. Weller [73] performed LES of a backward-facing step configuration and observed a slight improvement when a transport equation for  $\Xi$  was solved, compared to an algebraic, equilibrium approach. A correct prediction of  $\Xi$  in spark-ignition engines, where non-equilibrium effects like transition from laminar to turbulent flow occur, has been successfully achieved by Richard et al. [60] utilising a  $\Sigma$  transport equation; deviations from experimental data occurred here when equilibrium of wrinkling and turbulence were assumed. The use of a transport equation is also advocated by Driscoll [18] who assumes a memory of flame wrinkling and concludes that the influence of burner geometry on the flame wrinkling can only be properly predicted at all operating conditions when using a FSD transport equation. Further modelling approaches for a  $\Sigma$ –transport equation have been proposed by Hawkes et al. [30] and recently by Chakraborty et al. [9] with focus on Lewis number effects on the FSD. On the other hand, very good simulation results utilising algebraic LES models have been obtained e.g. by Fureby [22] in simulations of a dump combustor and a flame kernel growing in a combustion bomb and by Zimont et al. [74] in LES of a bluff body stabilised flame and a jet flame. Duwig et al. [20] successfully performed LES of a high pressure jet flame using an algebraic approach for the SGS flame wrinkling and a tabulated reaction rate including counter gradient transport. Moreover, algebraic flame wrinkling models in the thickened flame context as proposed by Charlette et al. [11] and Colin et al. [14] have been successfully applied in [32, 43]. The promising performance of algebraic LES combustion models compared to experimental data can justify the use of algebraic models, at least when only weak non equilibrium effects are expected or when a dynamic formulation of an algebraic model is used, as proposed by Hawkes et al. [31] and Charlette et al. [12] and as has been successfully applied by Wang et al. [72]. Several LES combustion models e.g. as summarised in Chakraborty and Klein [10] have a direct counterpart in the RANS context. This can be an advantage, since the extensive evaluation and review of RANS models e.g. by Lipatnikov and Chomiak [49], Veynante and Vervisch [71] or the series of papers on evaluation of combustion models by Bray et al. [5] provide a good basis for the judgement of the strengths and weaknesses of the modelling approaches and thus for model development. Hence, in this work, an already well performing RANS model is chosen as basis for the derivation of a new LES model. Lipatnikov and Chomiak [49] investigated several experimental databases and algebraic combustion models and found a very good performance of the Zimont model [75] and a promising performance of a first formulation of the fractal turbulent flame speed closure model of Gouldin et al. [26]. Bray, Champion and Libby [5] investigated five RANS models, among others the Zimont model [75] and a model using a transport equation for the FSD proposed in Veynante and Vervisch [71] by considering flames impinging on a wall. Only the model proposed by Lindstedt and

Váos [48], which is based on an enhanced version of the Gouldin TFC model, the so called chemical closure for the fractal approach of Gouldin et al. [27], showed good agreement with all experimental data used in the study of Bray et al. [5], results using this algebraic model here were superior than even those from a FSD transport equation model. Since Brandl et al. [4], Muppala et al. [54] (with an explicit pressure correction) and of course Lindstedt et al. [48] verified a good performance of the Lindstedt-Váos model by performing RANS simulations of Bunsen flames, isochoric vessels, counter flow flames and combustion in tubes, the Lindstedt-Váos model has been chosen to be the basis for the derivation of the present new LES model. Before deriving the LES model, the ideas of the fractal model developed by Gouldin et al. [27] in the RANS context are summarised and the modelling options for the fractal parameters based on DNS and experimental data and based on results from theoretical studies are discussed. An algebraic LES model is then derived, using the same physical concepts applied in the LES context. The original RANS model does not obey the correct behaviour in the low Re limit, and it does not take into account the effect of strain on the laminar flame speed. The proposed LES model is extended to cover the low Re regime and incorporates the linear theory of instabilities. The present work focuses on flow conditions typical for spark ignition conditions, i.e. low to moderate Reynolds number combustion, but is also applied successfully for highly turbulent flames characteristic for gas turbine combustors. In both applications a correct prediction of turbulent flame speed with varying pressure is important. As has been observed by Lipatnikov and Chomiak [49], the turbulent flame speed is nearly independent of pressure for methane/air flames. A similar observation was made by Duwig et al. [20], who validated a LES code using a high pressure jet configuration at conditions typical for stationary gas turbines, where the flow field is highly turbulent. The pressure independence of turbulent combustion is only valid for methane/air flames (turbulent propane air flames exhibit a distinct pressure dependence [49]). Since the correct scaling of turbulent flame speed with pressure is not trivial and is not reproduced by several combustion models proposed in the literature, the present model was validated employing the turbulent Bunsen flame database of Kobayashi et al. [39–41], simulating 25 different operation points at pressures ranging from 0.1 to 2 MPa. The simulated flames belong to the wrinkled and corrugated flamelets as well as thin reaction zones regimes and correspond to the typical range of spark ignition engines. Methane and propane fuels were used with air as oxidiser. The model is evaluated in terms of the predicted turbulent flame speed and the predicted flame surface for three systematically refined computational grids. To validate the new combustion model also for conditions typical for gas turbines, LES at different pressure levels of a highly turbulent jet flame, as experimentally investigated by Griebel et al. [28], are performed and results for the velocity field, turbulence field and the flame shape are compared. In the paper, we first present the physical concepts used to derive the fractal model of Gouldin et al. in the RANS context and we then derive the corresponding LES subgrid combustion model. The model is then extended into the low Re limit and to incorporate flame stretch effects. The numerical implementation into OpenFOAM is first verified using a 1-D propagation of laminar and turbulent flat flame fronts. The validation of the model using turbulent Bunsen and jet flames are then presented and grid effects are investigated. It is shown that the predicted turbulent flame speed is in good agreement with experiment, depends very weakly on grid size and scales correctly with pressure. Finally we give some conclusions.

## 2 Combustion Modelling

This work concentrates on perfectly premixed turbulent combustion. Following Poinso and Veynante [58], a Favre-filtered balance equation for the Favre filtered progress variable  $\tilde{c}$  can be derived in the LES context:

$$\frac{\partial \bar{\rho} \tilde{c}}{\partial t} + \frac{\partial \bar{\rho} \tilde{u}_i \tilde{c}}{\partial x_i} + \frac{\partial}{\partial x_i} (\bar{\rho} \tilde{u}_i \tilde{c} - \bar{\rho} \tilde{u}_i \tilde{c}) = \frac{\partial}{\partial x_i} \left( \bar{\rho} \alpha \frac{\partial \tilde{c}}{\partial x_i} \right) + \bar{\dot{\omega}}_c \quad (2)$$

where  $\alpha$  denotes the laminar diffusion coefficient. In Eq. 2 some assumptions are made: Heat loss effects are neglected and  $Le = 1$  is assumed if (2) is interpreted as balance equation for a reduced temperature variable. Following Boger et al. [3], the filtered molecular diffusion and the filtered reaction rate on the right hand side of Eq. 2 can be combined and described by a FSD formulation.

$$\frac{\partial}{\partial x_i} \left( \bar{\rho} \alpha \frac{\partial \tilde{c}}{\partial x_i} \right) + \bar{\dot{\omega}}_c \approx \rho_u s_L \Sigma \quad (3)$$

This type of modelling implies that the difference between laminar and turbulent flame speed is solely a result of the increased area of the thin flame surface, which propagates locally at the laminar flame speed  $s_L$ , but is folded by the turbulent eddies. A similar assumption is made in G-equation type models [56, 57], where an infinitely thin front is tracked as an isosurface of the G scalar. Also in the G equation approach, a turbulent flame speed subgrid model is required if not all flame wrinkling can be resolved on the numerical grid. The unresolved turbulent scalar flux is modelled here using the gradient assumption:

$$\bar{\rho} \tilde{u}_i \tilde{c} - \bar{\rho} \tilde{u}_i \tilde{c} = - \frac{\mu_{SGS}}{Sc_t} \frac{\partial \tilde{c}}{\partial x_i} \quad (4)$$

where  $Sc_t$  denotes the turbulent Schmidt number. Counter-gradient SGS fluxes, which might be noticeable at very low turbulence levels and low  $Re$  number are not explicitly modelled here. Contrary to RANS, where counter-gradient transport should be modelled (see Veynante et al. [70]), in LES the main part of the turbulent fluxes [63] and therefore possibly also of the counter-gradient fluxes are resolved (Boger et al. [2]), particularly at low  $Re$  conditions. In addition, the use of  $|\nabla \tilde{c}|$  instead of  $|\nabla \tilde{c}|$  in the LES modelling of  $\Sigma$  (as used here, see below) represents already a simple model of counter-gradient transport as shown in [44, 45]. With these assumptions, the transport equation for the Favre-filtered progress variable becomes:

$$\frac{\partial \bar{\rho} \tilde{c}}{\partial t} + \frac{\partial \bar{\rho} \tilde{u}_i \tilde{c}}{\partial x_i} = \frac{\partial}{\partial x_i} \left( \frac{\mu_{SGS}}{Sc_t} \frac{\partial \tilde{c}}{\partial x_i} \right) + \rho_u s_T |\nabla \tilde{c}| \quad (5)$$

with the following definition of the turbulent flame speed  $s_T$ :

$$s_T |\nabla \tilde{c}| = s_L \Sigma = s_L \Xi |\nabla \tilde{c}| \quad (6)$$

An integration of Eq. 5 from  $-\infty$  to  $\infty$  in the planar, one-dimensional case yields a mass burning rate of  $\rho_u s_T$ , which is solely controlled by the last, gradient-type source term on the RHS of Eq. 5, whereas the first, diffusion term on the RHS does not affect the mass burning rate [49]. For a planar, one-dimensional, constant density “flame” and for a (constant) velocity of unburnt gas  $u_x = s_T$ , Eq. 5 reduces to a standard diffusion equation

$$\frac{\partial \tilde{c}}{\partial t} = \frac{\partial}{\partial x} \left( D_T \frac{\partial \tilde{c}}{\partial x} \right) \quad (7)$$

In this case, the flame front is not moving and the flame brush thickness will continue to grow indefinitely due to turbulent diffusion with diffusion coefficient  $D_T = \frac{\mu_{SGS}}{\rho S_{c_t}}$ . This effect has been discussed extensively in the framework of the Zimont RANS model (see e.g. [75]) and can be observed experimentally in rod-stabilized flames [17, 66]. In most technical flames the turbulence decays relatively quickly along the flame length. In a LES, then more and more of the turbulent motions and of the flame wrinkling can be resolved. The broadening of the resolved flame brush will cease in the LES when all subgrid wrinkling can be fully resolved and  $\mu_{SGS}$  vanishes.

## 2.1 Modeling the filtered flame surface density

The fractal character of the turbulent folding of thin premixed flames is well known and has been well proved experimentally (see, e.g. [61]). While in a RANS model the whole range of flame folding between a smallest and a largest fractal length scale needs to be modelled, in LES only a model for the statistical process of the ensemble averaged, non resolved subgrid flame folding is required. Due to the fractal character of the wrinkled flame front, the LES subgrid model will retain the same mathematical form as the RANS combustion model, however with the RANS outer cut-off length (usually taken as the integral length scale) replaced with the largest scale resolved in the LES. LES fractal SGS flame wrinkling models based on Eq. 1 and assuming a power-law dependence of the flame wrinkling have been proposed by [10, 11, 31]. The wrinkling factor in these models assumes a form like in the fractal approach proposed by Gouldin [26]:

$$\Xi = \left( 1 + \frac{\epsilon_0}{\epsilon_i} \right)^{D-2} \quad (8)$$

$D - 2$  represents the scaling exponent  $\beta$  used in [11, 31].  $D$  can be interpreted as a fractal dimension.  $\epsilon_0$  denotes the largest (non resolved) wrinkling scale,  $\epsilon_i$  the smallest one. The value of 1 in the bracket is usually added to obtain a flame wrinkling factor near 1 when  $\epsilon_i > \epsilon_0$  [11]. A power-law dependency or fractal characteristics of the flame wrinkling factor  $\Xi$  on a ratio of the scales  $\epsilon_{i,0}$  is supported by evaluations of DNS-data [31], by several experimental studies e.g. [51, 61], and is also seen in theoretical studies of isosurfaces of an inert scalar in homogeneous and isotropic turbulence and a Kolmogorov energy cascade. While (8) can be used directly as a basis for a fractal model, the aim of this work is to derive a LES model which is close to the RANS approach proposed by Lindstedt and Váos [48] based on the (fractal) chemical closure approach of Gouldin et al. [27]. The RANS derivation of this model is shortly summarised in the following. A fractal character of the flame surface and a self-similar wrinkling of the surface between the cut-off scales  $\epsilon_{i,0}$  by turbulent motions is assumed. The flame surface  $A$  in a control volume  $L^3$ , wrinkled between an inner cut-off  $\epsilon_i$  and an outer cut-off  $\epsilon_0 = L$ , can be written as [26]:

$$\frac{A}{L^3} \sim \left( \frac{\epsilon_i}{L} \right)^{2-D} L^{-1} \quad (9)$$

Interpreting  $D$  in the exponent as a fractal dimension, it can vary between 2, when the unresolved surface is assumed to be smooth in the control volume i.e.  $\epsilon_i > \epsilon_0$  and 3 when the unresolved surface is assumed to be wrinkled in such a manner, that the control volume is completely filled. Gouldin et al. [27] introduce a probability density function:

$$p_c = C_p \tilde{c}(z) (1 - \tilde{c}(z)) \quad (10)$$

of finding a flamelet along the flame normal  $z$ . The probability should become 1, when integrated over the full flame brush thickness, so that the constant in Eq. 10 can be approximated by the inverse of the turbulent flame brush thickness.

$$p_c = \tilde{c}(1 - \tilde{c}) \frac{L}{\delta_t} \quad (11)$$

Introducing a proportionality model constant  $C_R$ , the FSD is finally written as:

$$\Sigma = C_R \left( \frac{\epsilon_i}{L} \right)^{2-D} \frac{\tilde{c}(1 - \tilde{c})}{\delta_t} \quad (12)$$

In RANS as well as in LES, Eq. 12 in conjunction with (3) represents a model of the ensemble-averaged increase of source term in the transport equation of the Favre-averaged progress variable  $\tilde{c}$  due to non-resolved folding of the flame. The probability density function based on a time or ensemble average in the RANS context to derive (10, 11) can be interpreted in the LES context as a filtered density function representing the ensemble averaged, non-resolved, fractal subgrid flame folding. While in RANS,  $\delta_t$  represents the full turbulent flame brush, in LES,  $\delta_t$  has to be interpreted as the locally resolved flame brush. The main assumption of the present LES model is that the ensemble average of the non resolved folding of the flame on the LES subgrid retains the same statistical fractal characteristics as the ensemble average in a corresponding RANS model and thus the same mathematical structure (see also discussion on connection between RANS and LES flame surface density models in Poinso and Veynante [58]). As is shown below, even in cases where the most of the turbulent energy of the flow field is resolved by the LES, a large part of the flame folding may still occur on the subgrid at high Re numbers. In such cases, the modelling task of the LES subgrid model is similar to that of a RANS model, if severe restrictions on the LES filter width / cell size should be avoided [69].

## 2.2 Modelling the outer cut-off scale $\epsilon_o$

Gouldin and Lindstedt in the RANS context applied the integral length scale  $l_t$  to describe the outer cut-off, arguing, that this is not the largest scale but the one, that carries most of the turbulent energy. Some experimental evidence showing that the largest wrinkling scale of the fractal range is similar to the integral length scale can be found in North et al. [61]. In LES, the outer cut-off represents the largest wrinkling length scale which cannot be resolved numerically. Usually the filter width  $\Delta$  is chosen. It is assumed here, that similar to the Nyquist criteria, at least 2 cells are needed to resolve a wrinkling of the flame front. The outer cut-off scale is thus modelled as:

$$L = 2.2\Delta \quad (13)$$

Since in a LES the filter width should be well within the integral subrange,  $2.2\Delta \leq l_t$  should be satisfied automatically. In addition, a LES should resolve about 80 % of the turbulent kinetic energy, which usually leads to  $\Delta \ll l_t$ . When using a non-oscillatory numerical scheme to solve the progress variable transport equation, the resolved flame front may be thicker than 2 cells due to nonlinear numerical diffusion introduced by these discretization schemes near strong gradients. It is argued here, that a transverse wrinkling of the flame front can still be resolved in about 2 cells, since the nonlinear artificial diffusion in non-oscillatory schemes acts only normal to the flame front and the momentum equations providing the velocity field wrinkling the flame are not discretized using TVD schemes in LES simulations.



### 2.3 Modelling the inner cut-off scale $\epsilon_i$

Lindstedt et al. [48] and Gouldin [26] applied the Kolmogorov scale

$$\epsilon_i = \eta = Ka^{-1/2} l_F \quad (14)$$

with the Karlovitz number  $Ka$  to model the inner cut-off. The laminar flame thickness is modelled via  $l_F = D_{th}/s_L^0$  and assuming a Schmidt number of  $Sc = 1$ . Peters [56] argued, that  $\epsilon_i$  scales with the Kolmogorov scale only within the thin reaction zone regime and with the Gibson scale within the corrugated regime:

$$\epsilon_i = l_G = \left(\frac{s_L}{u'}\right)^3 l_t \quad (15)$$

The Peters proposal is supported by evaluation of DNS-data by Chakraborty and Klein [10] where  $\epsilon_i$  exhibits different scalings with  $Ka$  in the corrugated flamelet and the thin reaction zone regime. Therefore, the model for the inner cut-off, proposed in [10] utilises a blending function to switch between both expressions dependent on the Karlovitz number. Also Hawkes et al. [31] applies a combination of the Gibson scale and the Obukhov-Corrsin scale, which reduces to the Kolmogorov scale assuming unity Schmidt number [56]. On the other hand, based on DNS-data Poinso et al. [59] identified an inner cut-off scale, which is independent of the combustion regime and scales with  $\epsilon_i \sim Ka^{-1/3}$  [29]. Furthermore Gülder and Smallwood [29] investigated numerous experimental data sets and concluded, that the nondimensional inner cut-off scale  $\epsilon_i/l_F$  scales solely with the Karlovitz number  $Ka^\beta$ , where  $\beta$  is a constant between  $-1/2 \leq \beta \leq -1/3$ . Additionally, the experimental data summarised in [29] does not show a change in scaling in the different combustion regimes. A scaling with  $Ka^{-1/2}$  is supported by Constantin et al. [15], who obtained a scaling for the inner cut-off scale with the Kolmogorov scale performing Lagrangian calculations and studying experimental data of isothermal surfaces in a turbulent medium. Finally, the evaluation of the inner cut-off scale for the Kobayashi database in [42], where Bunsen flames are investigated which belong to the wrinkled, corrugated and thin reaction zone regime, indicate a scaling of about  $\epsilon_i \sim l_F Ka^{-1/2}$ . In the wrinkled flamelet regime, the speed of turbulent motions is assumed to be too slow to wrinkle a flame [56, 58]. Experimental data of Smallwood [65] and Das [16] depicted in [29] include measurements characterised by  $u'/s_L^0 < 1$ , which show the same scaling of  $\epsilon_i \sim l_F Ka^\beta$  in the wrinkled flamelet regime as well as in the corrugated and thin reaction zone regime. Also the  $\epsilon_i$  scaling evaluated employing the Kobayashi database in [42], where several investigated operation points exhibit  $u'/u_l^0 < 1$  show a scaling of about  $\epsilon_i \sim l_F Ka^{-1/2}$ . Based on the experimental findings in [29, 42] and to keep a similar scaling like in the RANS Lindsted-Vaas model [48] it has been decided to apply

$$\epsilon_i \sim l_F Ka_\Delta^{-1/2} \quad (16)$$

where the subgrid Karlovitz number is defined as:

$$Ka_\Delta = \left(\frac{u'_\Delta}{s_L^0}\right)^{3/2} \left(\frac{\Delta}{l_F}\right)^{-1/2} \quad (17)$$

With  $\Delta$  within the inertial range as is required for a good LES,  $Ka_\Delta$  is approximately independent of  $\Delta$ , since here  $(u'_\Delta/\Delta)$  is proportional to dissipation rate  $\epsilon$ , which is constant in the inertial range. Equation 16 can predict an inner cut-off length smaller than the laminar flame thickness. Driscoll [18] summarised experimental data showing that the smallest wrinkling scale is larger than  $const. \cdot l_F$ , where  $const.$  is of the order of one. Kobayashi et al. [42] stated, that at least for high pressure turbulent flames, a constant value

for  $\epsilon_i/l_F$  is reached. Here,  $\epsilon_i$  is therefore limited to a value proportional to  $l_F$  and is written as:

$$\epsilon_i = l_F \max \left( Ka_{\Delta}^{-1/2}, 2 \right) \quad (18)$$

## 2.4 Modelling the fractal dimension $D$

The exponent  $D = \beta - 2$  in Eq. 8 incorporates the fractal dimension, assuming a power-law dependency of the subgrid flame wrinkling on the ratio of  $\epsilon_0$  to  $\epsilon_i$ . In most previous models,  $D$  is assumed to be constant. Charlette et al. [11] applied a value of  $D = 2.5$ , Lindstedt and Váos [48], Tangermann et al. [67], Kerstein [37] and Muppala et al. [54] used a value of about 7/3 and Gouldin [26] recommended values of about 2.32–2.4 based on experimental data. However, experimental data presented in North and Smallwood [61], Kobayashi et al. [42], Marayama [55] and Goix et al. [24] indicate a dependency of  $D$  on  $u'/s_L^0$  or in the latter case on the downstream distance from burner exit. An increase of  $D$  from the corrugated flamelet regime to the thin reaction zone regime has been detected evaluating DNS in Chakraborty et al. [10] and the reported values are in good agreement with the correlation proposed in [61]. Chakraborty et al. [10] proposed an expression for  $D$  dependent on  $Ka$ :  $D = 2 + (1/3)\text{erf}(2Ka)$ , which varies from 2 in the corrugated regime to 7/3 in the thin reaction zone regime. A dependency of  $D$  on  $Ka$  is supported by Hawkes et al. [31], who claimed that  $D$  (as well as  $\epsilon_i$ ) should be interpreted as physical parameters, assuming (8) to be correct, and therefore (at least theoretically)  $D$  should be modelled independent of the filter size [31]. Of course, this would be only true defining  $Ka$  as  $Ka = l_F^2/\eta^2$ . The evaluation of  $D$  in [31] is mainly based on theoretical considerations of the behaviour of the flame wrinkling factor in Damköhler's small- and large-scale limit. An expression of  $D$  has been derived in [31] including the Gibson scale and the Obukhov-Corrsin scale. Applying this expression,  $D$  varies from 7/3 for Damköhler's large-scale limit, to 8/3 for Damköhler's small-scale limit. A theoretical model of the fractal dimension for combustion has been proposed by Giacomazzi et al. [7]. It has been derived, assuming an energy cascade in each LES cell and yields the Kolmogorov cascade in the limit of isothermal flow. The model, slightly modified, has been successfully applied in [36] to simulate a turbulent Bunsen flame and is written as:

$$D = \min \left( 1 + \frac{\ln \left( \pi^{-2/3} Re_{\Delta} (v_u/v_b) \right)}{\ln \left( \pi^{1/6} Re_{\Delta}^{1/2} (v_u/v_b)^{1/2} \right)}, 8/3 \right) \quad (19)$$

Here the fractal dimension is limited to a value of 8/3, since  $D$  according to Eq. 19 approaches 3 in the limit of  $Re_{\Delta} \rightarrow \infty$ . Additionally, the ratio of the kinematic viscosity of the unburned mixture  $v_u$  to the burned mixture  $v_b$  has been introduced, to account for influence of heat release on the turbulence within the LES cell to a limited extent. This extension has been identified to be necessary to obtain the promising simulation results compared to experimental data in [36]. However, Eq. 19 depends on the Reynolds number, which leads to a resolution or filter size dependency of the fractal dimension which should be avoided following Hawkes et al. [31], as argued above. Therefore, in this work (19) has been replaced by an expression of  $D$ , dependent only on  $Ka_{\Delta}$ .

$$D = \frac{8/3 Ka_{\Delta} + 2c_D}{Ka_{\Delta} + c_D} \quad (20)$$

The constant  $c_D$  has been chosen as 0.03, to give a good agreement with (19) for equal turbulence and pressure levels. Equation 19 varies between 2 and 8/3. The upper value has been

chosen in agreement with in [31]. To the best of our knowledge and as already stated in [31], there is no direct experimental data from premixed combustion test results that supports an upper value of about  $8/3$ . On the other hand, the proposed upper value is consistent with statistical and kinematic arguments, considering the energy spectrum of isotropic Kolmogorov turbulence, as stated by Mandelbrot et al. [51] and the DNS data of Hawkes et al. [31]. Constantin et al. [15] clarified this discrepancy somewhat, by identifying upper values of  $D$  of about 2.67 in the fully turbulent inner region of a jet and maximum  $D$  values of about 2.33 in the region mainly influenced by the boundaries of the jet by Lagrangian calculations as well as experimental investigations of non-reacting flow. Klimenko [38] finally argued that downstream of the flame a cascade hypothesis with  $D = 7/3$  is more correct, which does not exclude, that upstream of the flame the Kolmogorov hypothesis with a fractal dimension of about  $D = 8/3$  might be valid<sup>1</sup>. A more practical justification for  $D_{\max} = 8/3$  in the context of pressure dependency in the limit of high  $u'$  values, is obtained by investigating the combustion model in the limit of a planar flame, propagating in frozen turbulence. Performing a KPP-analysis of the presented LES combustion model as described e.g. in Poinso and Veynante [58] and applying Eqs. 18 and 17, the turbulent flame speed  $s_t$  of the combustion model for a planar flame becomes:

$$s_t = 2 \cdot \left( \left( \frac{\nu_{SGS}}{S_{c_t}} \right) \frac{C_R \cdot s_L^0}{\delta_t} \left( \frac{2.2 \Delta \cdot u'_{\Delta}}{C_{\epsilon,i} \cdot \nu} \right)^{0.75 \cdot (D-2)} \right)^{0.5} \quad (21)$$

The turbulent diffusivity has been replaced by  $\nu_{SGS}$ , which is assumed to depend only on turbulent fluctuations and the integral length scale [49]. For discussion of Eq. 21 it is further assumed, that the turbulent flame brush thickness  $\delta_t$ , e.g. as summarised by Lipatnikov and Chomiak [49] can be described by the Taylor theory of turbulent diffusion:

$$\delta_t \sim \begin{cases} u't & \text{if } t \ll l_t/u' \\ \sqrt{2u'l_t t} & \text{if } t \gg l_t/u' \end{cases} \quad (22)$$

and for intermediate times:

$$\delta_t \sim \sqrt{2u'l_t t \left[ 1 - \frac{l_t/u'}{t} \left( 1 - \exp \left( -\frac{t}{l_t/u'} \right) \right) \right]} \quad (23)$$

where  $l_t/u'$  has been applied to approximate the Lagrangian time scale. Equations 22, 23 show that growing of  $\delta_t$  only depend on time or downstream distance and turbulence level but does not incorporate thermo-physical properties which depend on pressure. This is supported by evaluation of the turbulent flame brush thickness at similar turbulence but different pressure levels in Lee et al. [46] where no correlation between flame brush thickness and pressure is found by the authors. Hence, for the following discussion with focus on pressure dependency of  $s_t$  at high turbulence level,  $\delta_t$  and  $u'$  is kept constant. According to Lipatnikov and Chomiak [49], for methane the turbulent flame speed does not scale with pressure i.e.  $s_t \sim p^0$ . Griebel et al. [28] confirmed the pressure independence of  $s_t$  for methane from experimental investigations of a high Reynolds number jet flame. Since the pressure scaling for methane mixture of the laminar flame speed is  $s_L^0 \sim p^{-0.5}$  [49] and  $\nu \sim p^{-1}$ , the fractal dimension has to reach a constant upper value of about  $8/3$  in the limit of high Reynolds number combustion to predict the correct pressure scaling of the turbulent flame speed using the presented model.

<sup>1</sup>We thank Alexander Klimenko for the helpful discussion, clarifying this point

## 2.5 Modelling the turbulent flame brush thickness

In the RANS context, Lindstedt and Sakthitharan [47] proposed to model the turbulent flame brush thickness  $\delta_t$  to be proportional to the integral length scale. In LES, a simple representation of the resolved flame brush thickness  $\delta_t$  by the filter width would clearly be an underestimate as shown below. In this paper we therefore estimate  $\delta_t$  locally, assuming that the  $\tilde{c}$  dependence of the resolved flame brush has a similar shape as that of a fully developed turbulent flame brush. It is shown later that this assumption is not necessary any more in a simplified model proposed below. Using the maximum gradient method [50] in flame normal direction  $z$ , the turbulent flame brush thickness can be estimated via:

$$\delta_t^{-1} = \max \left( \frac{d\tilde{c}}{dz} \right) \quad (24)$$

As described in detail in Lipatnikov and Chomiak [49, 50], normalising the flame normal direction with  $\delta_t$  yields an universal profile as function of the progress variable  $\tilde{c} / \tilde{c}$ , that is approximated very well by the complementary error function.

$$\tilde{c}(\xi) = 1 - \frac{1}{2} \operatorname{erfc}(\xi \sqrt{\pi}) \quad (25)$$

where  $\xi$  denotes the normalised flame normal direction  $\xi = (z - z_0)/\delta_t$ . Differentiating (25) with respect to  $\xi$  yields the slope of  $\tilde{c}$  [6]:

$$F(\tilde{c}(\xi)) \equiv \frac{d\tilde{c}}{d\xi} = e^{-\pi\xi^2} \quad (26)$$

Eliminating  $\xi$  from Eqs. 25, 26 yields the  $F(\tilde{c})$ , the slope of the universal flame brush as function of  $\tilde{c}$ :

$$F(\tilde{c}) = e^{-[\operatorname{erfc}^{-1}(2(1-\tilde{c}))]^2} \quad (27)$$

$F(\tilde{c})$  allows the computation of  $\partial\tilde{c}/\partial z$  vs.  $\tilde{c}$ , and using (24),  $\delta_t^{-1}$  can be approximated by  $|\nabla\tilde{c}|/F(\tilde{c})$ . In the numerical implementation,  $F(\tilde{c})$  is approximated by a simple polynomial fit:  $F(\tilde{c}) \approx a1 - a2(\tilde{c} - 0.5)^2 - a3(\tilde{c} - 0.5)^4$  with  $a1 = 0.995176$ ,  $a2 = 2.81811$ ,  $a3 = 4.30724$  and  $|\nabla\tilde{c}|$  is evaluated from the instantaneous  $\tilde{c}$  field.

## 2.6 Final model formulation

Combining all parts of the model yields the final model for the flame surface density  $\Sigma$ :

$$\Sigma = C_R \cdot \left( \frac{2.2\Delta}{\max(l_F K a_\Delta^{-1/2}, 2l_F)} \right)^{D-2} \tilde{c}(1 - \tilde{c})F(\tilde{c})^{-1}|\nabla\tilde{c}| \quad (28)$$

The equation contains a model constant  $C_R$ . A value of  $C_R = 4.5$  is chosen for a best fit to experimental data, see Sections 4.3.3 and 5.3.

## 2.7 Model variants

### 2.7.1 Use of blending function

In principle, any FSD model should reduce exactly to  $|\nabla\tilde{c}|$  in the limit of fully resolved wrinkling ( $\Delta \rightarrow 0$  and  $u'_\Delta \rightarrow 0$ ) (see e.g. [10]). In these limits,  $[C_R\tilde{c}(1 - \tilde{c})F(\tilde{c})^{-1}]$  in Eq. 28 becomes about 1.1 at  $\tilde{c} = 0.5$  for  $C_R = 4.5$  and the term  $(\dots)^{D-2}$  in Eq. 28 becomes 1. A slight reduction of  $C_R$  to achieve the correct limit would worsen the agreement

of simulation results with experimental validation data. Therefore, in the limit of zero filter size the theoretically exact behaviour of Eq. 28 is achieved by incorporation of a blending function as proposed by Chakraborty and Klein [10]:

$$\Sigma = \left\{ \exp\left(-\frac{\Delta}{\epsilon_i}\Theta\right) + \left(1 - \exp\left(-\frac{\Delta}{\epsilon_i}\Theta\right)\right) C_R \left(\frac{2.2\Delta}{\max(l_F \cdot K a_{\Delta}^{-1/2}, 2l_F)}\right)^{D-2} \tilde{c}(1 - \tilde{c})F(\tilde{c})^{-1} \right\} |\nabla \tilde{c}| \quad (29)$$

$\epsilon_i$  is modelled using (18). Following [10] we choose the constant in the blending function as:  $\Theta = 2.5$ . There were no noticeable changes in the results of validation simulations when using either the model from Eqs. 28 or 29. Differences will only show up in very low Re flames, where all flame folding is resolved anyway.

### 2.7.2 Simplified model

The model (28) can be simplified by noting that the term  $\tilde{c}(1 - \tilde{c})F(\tilde{c})^{-1}$  in Eq. 28 is nearly constant with a value of about 0.22 over the whole range of  $\tilde{c}$ . Figure 1 shows curves of  $\tilde{c}(1 - \tilde{c})$ ,  $F(\tilde{c})$  and  $\tilde{c}(1 - \tilde{c})F(\tilde{c})^{-1}$  vs.  $\tilde{c}$ .

Using  $C_R \approx 4.5$ ,  $C_R \tilde{c}(1 - \tilde{c})F(\tilde{c})^{-1} \approx 1$  yields a combustion model without any model constant:

$$\Sigma = \left(\frac{2.2\Delta}{\max(l_F K a_{\Delta}^{-1/2}, 2l_F)}\right)^{D-2} |\nabla \tilde{c}| \quad (30)$$

Note that this simpler parameter free model obeys the correct behaviour in the limit of fully resolved flame wrinkling ( $\Delta \rightarrow 0$  or  $u'_{\Delta} \rightarrow 0$ ), but the agreement with validation data would be slightly worse for this model. The simplified model, however, allows an analytical evaluation of the wrinkling factor  $\Xi$  independent of the numerical  $\tilde{c}$  solution due to the

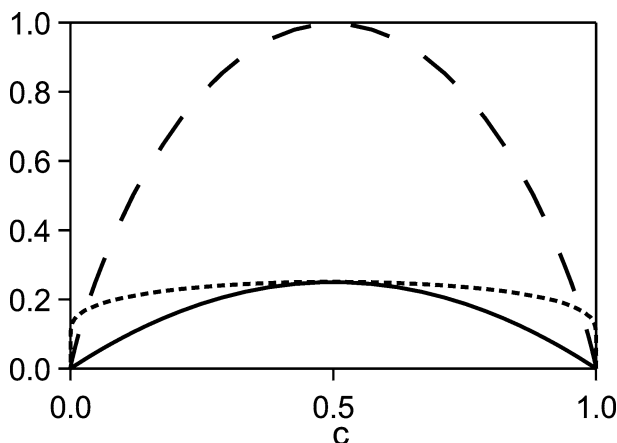


**Fig. 1** Evaluation of  $\tilde{c}(1 - \tilde{c})$ : solid line;  $F(\tilde{c})$ : dashed line;  $\tilde{c}(1 - \tilde{c})F(\tilde{c})^{-1}$ : dotted line; The evaluation shows, that the expression  $\tilde{c}(1 - \tilde{c})F(\tilde{c})^{-1}$  is nearly independent of  $\tilde{c}$

absence of the terms  $\tilde{c}(1 - \tilde{c})F(\tilde{c})^{-1}$  in the expression of  $\Sigma$ , thus allowing a comparison of analytical and numerical solutions of the transport equation.

## 2.8 Modelling the laminar flame speed

The unstretched laminar flame speed  $s_L^0$  is calculated according to correlations derived by Müller et al. [53] and Göttgens et al. [25]. To account for stretch effects on the laminar flame speed, the linear theory of instabilities [13] is applied.

$$s_L = s_L^0 - Ma_c \kappa \cdot l_F \quad (31)$$

where the Markstein number  $Ma_c$  is calculated based on correlations in [53]. The disturbed laminar flame speed is bounded by a minimum value of  $s_L = 0$ . As stated by Lipatnikov and Chomiak [49], this theory is only valid for  $D_{th,u}/s_L^0 \cdot \kappa \ll 1$ , where  $D_{th,u}$  denotes the thermal diffusivity of the unburned mixture and is therefore only valid for weakly perturbed flames. But as has also been stated in [49], employing (31) is an often used practice and easy to implement. The stretch  $\kappa$  is computed here neglecting curvature effects. This is based on the argument that in the mean, curvature effects may be neglected [58]. Additionally, test simulations have shown that the curvature numerically computed from the  $\tilde{c}$  field of a completely spherical flame front (1) depends on the angle between flame normal direction and cell normal direction and (2) can overestimate the actual curvature by about 10 %. It is argued here, that neglecting curvature effects on the laminar flame speed will introduce smaller errors than incorporating an explicit, but inaccurate, curvature contribution. Strain effects, denoted as  $\kappa_S$ , are calculated based on strain resulting from the resolved flow  $\kappa_{mean}$  and strain resulting from the unresolved scales  $\kappa_{SGS}$  utilising a modified efficiency function  $\Gamma$ , as proposed by [52] and applied by Hawkes et al. [30]:

$$\kappa \approx \kappa_s = \underbrace{(\delta_{ij} - n_{ij}) \frac{\partial \tilde{u}_i}{\partial x_j}}_{\kappa_{mean}} + \underbrace{\Gamma \left( \frac{k_{SGS}}{s_L^0}, \frac{l_F}{\Delta} \right) \frac{\sqrt{k_{SGS}}}{\Delta}}_{\kappa_{SGS}} \quad (32)$$

with the Kronecker delta  $\delta_{ij}$ , the normalized flame normal  $n_{ij}$ , the  $SGS$  turbulent kinetic energy  $k_{SGS}$  and:

$$\log_{10}(\Gamma) = -\frac{1}{s+0.4} \exp(-(s+0.4)) + (1 - \exp(-(s+0.4))) \left( \sigma \left( \frac{u'_\Delta}{s_L^0} \right) s - 0.11 \right) \quad (33)$$

$$s = \log_{10} \left( \frac{\Delta}{l_F} \right); \quad \sigma \left( \frac{u'_\Delta}{s_L^0} \right) = \frac{2}{3} \left( 1 - 0.5 \exp \left( - \left( \frac{u'_\Delta}{s_L^0} \right)^{1/3} \right) \right); \quad u'_\Delta = \left( \frac{2}{3} k_{SGS} \right)^{0.5} \quad (34)$$

## 3 Tests of the Numerical Implementation of the Proposed Model

### 3.1 Implementation into OpenFOAM

The proposed model has been implemented into the open source library OpenFOAM®-1.6. Due to the low flow field velocities, a pressure based solver is applied, which yield a pressure field. The conservation of energy is taken into account solving an equation for

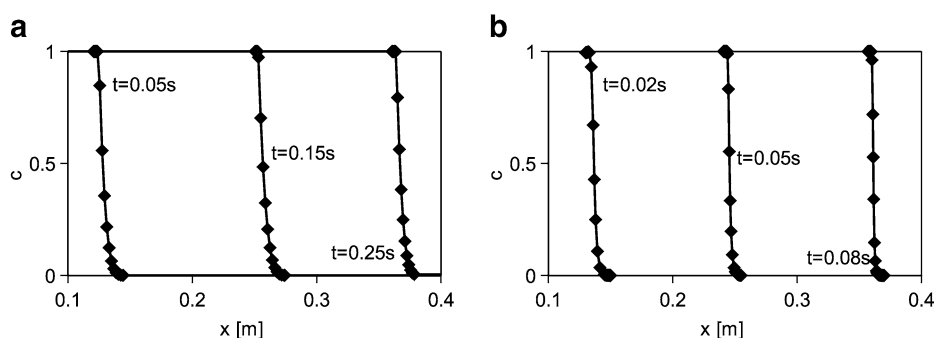


**Fig. 2** 1-D Simulation of a flat flame propagating through a channel; **a)**  $u'/s_L^0 = 0$ ; **b)**  $u'/s_L^0 = 0.5$ ; black diamonds show the grid points

the filtered enthalpy  $\tilde{h}$ . Filtered temperature  $\tilde{T}$  is then evaluated from  $\tilde{h}$  and  $\tilde{c}$  via JANAF polynomials assuming a one-step reaction. Filtered density  $\bar{\rho}$  is calculated from pressure, temperature and reaction progress using the ideal gas equation of state. No effects from subgrid fluctuations are taken into account in the calculation of filtered temperature and density.

### 3.2 Simulations of unsteady 1-D flame propagation

Simulations of the propagation of 1-D flat flame fronts (laminar and turbulent where all flame folding is subgrid) are performed to check whether the combustion model in combination with the numerical implementation is able to predict a reasonable flame propagation and the correct flame speed in the laminar and turbulent cases. To solely investigate the proposed FSD model, the unstretched laminar flame speed  $s_L^0$  is applied and turbulent diffusion is neglected. The filter width, equal to the mesh size, is set to  $\Delta = 0.5 \text{ mm}$ . Two-point backward differencing in time is applied. For numerical stability and accuracy the maximum Courant number is set to 0.3. The convective term of the momentum equation is discretized by an unlimited second order linear scheme. The convective term in the scalar transport is discretized by a second order linear scheme, applying a flux limiter, denoted “limitedLinear”<sup>2</sup> [33] to overcome oscillations due to large gradients at the flame front. The diffusive terms are discretized by a second order linear scheme. Figure 2a shows the simulation result of a laminar flame i.e.  $u'/s_L^0 = 0$  propagating through a 1-D channel, at 1 bar. The configuration has been initialised as burned on the left boundary and unburnt in the whole domain.

The flame thickness is numerically resolved by about 5–6 cells and it remains constant during propagation through the whole domain. The flame propagates at the correct laminar flame speed  $s_L$ . Near the boundaries  $x = 0 \text{ m}$  and  $x = 0.5 \text{ m}$  the flame thickness gets slightly reduced due to boundary effects. The propagation of a turbulent flame through the channel at  $p = 1 \text{ bar}$  and  $u'/s_L^0 = 0.5$  is shown in Fig. 2b. For this case, all flame wrinkling is subgrid, and the turbulent viscosity is set to zero to separate a possible numerical broadening of the flame from turbulent diffusion effects. Due to the increased subgrid flame wrinkling  $\Xi$ , the flame travels the same distance as in the laminar case in about 1/3 of this time. The turbulent flame front is also resolved within about 5–6 cells and the flame brush thickness and the flame form stay nearly constant.

<sup>2</sup>the coefficient is set to 0.5 as a compromise for best accuracy and convergence

### 3.3 Comments on model properties

It should be mentioned here, that when using the model transport (5), the molecular diffusion, molecular heat conduction and explicit chemical reaction terms have vanished from the modelled  $\tilde{c}$  transport equation. Thus the natural laminar flame thickness and form cannot be recovered by models of this type even on arbitrarily fine computational grids. Instead the numerically simulated flame thickness of a laminar flame front will continue to reduce as the grid is refined with a roughly constant number of grid points within the flame front. Our implementation of Eq. 2 using non-oscillatory discretization schemes will resolve the flame front in not less than 4–5 grid cells due to nonlinear artificial diffusion acting normal to sharp gradients. At high Re numbers (with a Kolmogorov length scale smaller than the physical flame thickness) on very fine grids with filter size below the natural flame thickness, this may lead to an artificial (resolved) wrinkling of the flame front, which is not observed experimentally [18]. However, this would occur only on computational grids with cell sizes much smaller than 0.1 mm (approaching a DNS grid resolution for most flames). Thus this restriction will not be of importance in most practical LES simulation situations. The LES model should ensure obviously that a laminar flame front propagates at the correct laminar flame speed in the limit of no subgrid flame folding and that there is no subgrid contribution to flame folding in regions where all flame wrinkling is resolved numerically. Both requirements are fulfilled in the present model. Extinction and differential diffusion effects could be implemented via additional terms in  $s_L$ . In models using Arrhenius reaction rates with detailed or reduced chemical mechanisms and laminar diffusion, the chemical source terms are very large and concentrated in narrow regions around the flame front. The correct laminar flame speed can be reproduced only on grids that can numerically resolve the laminar flame front. On the coarser grids typically used in LES, models of the artificially thickened flame (ATF) type [14] artificially increase the diffusion coefficient and decrease the chemical reaction rate such that the same flame speed is achieved but the flame front thickness is increased to become resolvable on the LES grid. In addition, a model (called efficiency function) is used here as well to account for the increased consumption rate due to non-resolved subgrid flame wrinkling. In some newer implementations of the ATF model, the modification of diffusion and reaction rate is only applied locally near flame front to avoid an overdiffusive solution elsewhere.

### 3.4 Simulations of stationary flames

In addition to the unsteady 1-D simulations, stationary simulations of 1-D flat flames and of 3-D laminar Bunsen flames are performed to show the effect of filter size on flame speed and to compare the flame speeds predicted by the different model formulations for the flame surface density  $\Sigma$  (28–30). The flames are initialised to be in the middle of a 1-D channel which has a length of 0.5 m. The velocity, temperature and progress variable fields are initialised as proposed by Poinot and Veynante [58] for laminar flame speed simulation, based on the analytical model proposed by Echehki and Ferziger [21]:

$$\tilde{c} \sim \begin{cases} (1 - 1/\beta_{Zel}) e^{x/l_F} & \text{if } x < 0 \\ 1 - 1/\beta_{Zel} e^{(1-\beta_{Zel})x/l_F} & \text{if } x > 0 \end{cases} \quad (35)$$

where  $x = 0$  corresponds to the critical reduced temperature defined as  $c_c = 1 - 1/\beta_{Zel}$ . The initial turbulent flame thickness is adjusted to about 5 mesh cells, which is the resolution



of a laminar flame front in the present implementation. The temperature is computed from  $T(x) = c(T_b - T_u) + T_u$  and the velocity field is initialised by:

$$U(x) = s_t + s_t(T/T_u - 1) \quad (36)$$

The turbulent flame speed is determined by:

$$s_t = \frac{\int_{-\infty}^{+\infty} \dot{\omega}_c dx}{\rho_u} \quad (37)$$

For each simulation case, a test simulation has been performed to evaluate the predicted  $s_t$ , which is then set as inlet velocity for a second run to confirm the predicted  $s_t$ . The evaluation of  $s_T$  according to Eq. 37 proved to be insensitive to this procedure. Results for the wrinkling factor  $\Xi = s_t/s_L$  from numerical 1-D simulations using the models presented in Eqs. 28, 29 are plotted in Fig. 3 as function of  $u'_\Delta/s_L$  along with an analytic evaluation of  $s_t/s_L$  from the simplified model (30). Results are shown choosing model parameters corresponding to methane flames at  $p = 1$  bar and  $p = 20$  bar. It can be seen that the analytical results and the data from the numerical simulations agree well, proving that the difference between the models is minor. In addition, the effect of refinement of the grid was studied in this 1-D setup. Figure 4 shows plots of the flame front from simulations on a coarse and a refined grid for laminar (left) and turbulent (right) flame propagation. The flame thickness is seen to decrease with grid refinement. Since the flame stayed stationary on both grids at the same inflow velocity of the unburnt mixture (which was set to the expected flame speed), the results prove that the flame propagation speed is not affected by the refinement of the grid and thus the numerical diffusion introduced by the numerical discretization scheme in this 1-D case.

To prove the ability of the implementation to reproduce the correct laminar flame speed in 3-D on differently fine grids, Fig. 5 shows colour contours and a  $\bar{c} = 0.5$  isoline (black) of the reaction progress from 3-D simulations of a laminar Bunsen flame on a coarse and a fine grid with an cell size ratio of about 2. The subgrid fluctuation and thus the turbulent diffusion terms were set to zero in these simulations. The numerical evaluation of the flame speed from these simulations gave: coarse grid:  $s_L = 0.3513$  m/s, fine grid:  $s_L = 0.3506$  m/s, exact:  $s_L = 0.35$  m/s. The method to evaluate the flame speed is the same as for the validation cases and is described below.

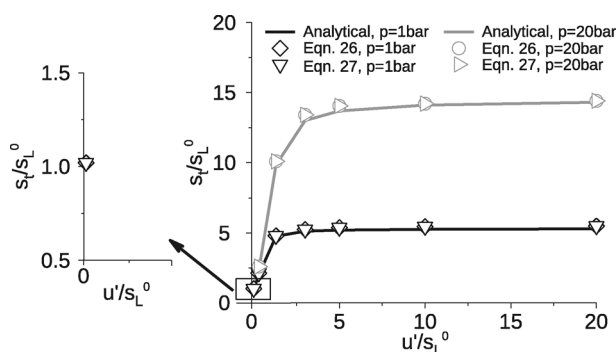


**Fig. 3** Evaluation of turbulent flame speed via 1-D simulation: Comparison of turbulent flame speed obtained from the analytical evaluation of Eq. 30 (line) and from 1-D simulation of flames using Eq. 28 (diamonds, circle) and Eq. 29 (triangles); parameters chosen corresponding to methane flames at  $p = 1$  bar (black) and  $p=20$  bar (grey)

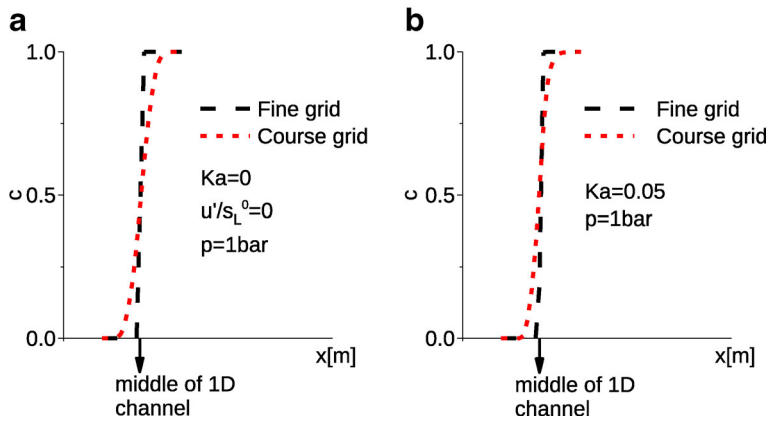


**Fig. 4** 1-D simulation of a stationary flame front at the middle of channel with coarse (*red*) and fine (*black*) grids; *left*  $Ka_{\Delta} = 0$  *right*  $Ka_{\Delta} = 0.05$

### 3.5 Conclusions regarding numerical implementation and test simulations

Some conclusions can be drawn from these results:

- The model is able to exactly reproduce the laminar flame speed in the limit  $u' \rightarrow 0$ , where  $\Sigma$  reduces to  $|\nabla \tilde{c}|$ .
- The model predicts an increase of subgrid flame wrinkling with increasing turbulence level.
- Some bending of the subgrid flame wrinkling is achieved at elevated turbulence level.

In the results presented in the following chapters, the full model (29) is used.

## 4 Simulation of a Turbulent Bunsen Flame

To validate the new combustion model at operation points typical for spark ignition engines and for different fuels, the database of Kobayashi et al. [39–41] is employed which covers moderate and low Reynolds number combustion. The database has already been

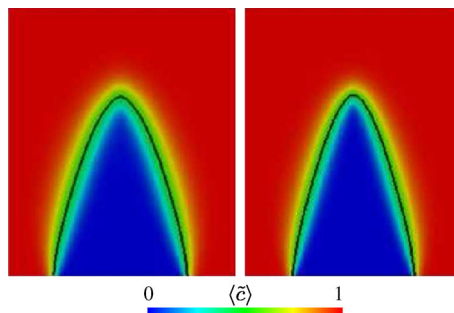


**Fig. 5** Evaluation of laminar flame speed by via 3-D simulation: Influence of filter size on the mean progress variable and instantaneous progress variable; *left* coarse grid *right* fine grid

simulated e.g. by Muppala et al. [54] and Brandl et al. [4] in RANS context and by Aluri et al. [1] in LES context.

#### 4.1 Experimental setup

In the experiments, a cone-shaped, premixed turbulent Bunsen flame is studied, burning in a high pressure chamber. 40 mm upstream of the burner nozzle, (diameter 20 mm) four different perforated grids can be installed to adjust a certain turbulence level and length scale. Turbulence levels and flow velocity in stream wise direction were measured by a hot-wire anemometer at the center of the nozzle. At the nozzle outlet, the flame is stabilised by a small pilot  $H_2$  diffusion flame. Inner diameter and length of the combustion chamber are 498 and 600 mm. A pressure sensor in combination with an automatic exhaust valve allows a constant pressure level during the measurements. Measurements have been carried out at pressure levels between 0.1 and 3 MPa. Flow velocity varies between 0.86 and 8.86 m/s, measured rms-values and integral length scales vary between  $0.0 \leq u' \leq 2.06$  m/s and  $0.7 \leq l_t \leq 1.9$  mm. Methane ( $\Phi = 0.9$ ), propane ( $\Phi = 0.9$ ) and ethane ( $\Phi = 0.5$ ,  $\Phi = 0.7$ ,  $\Phi = 0.9$ ) fuels were investigated. Photographic images were taken from the instantaneous flame. Assuming rotational symmetry, 50 instantaneous pictures were used to create an averaged flame front, which is reported to be equivalent to  $\bar{c} = 0.5$ . It has been claimed in [39], that apart from the tip and near the nozzle exit, the flame exhibits a constant slope, leading to the following conventional approach for estimating the turbulent flame speed:

$$s_t = U \sin(\varphi/2) \quad (38)$$

where  $U$  denotes the bulk velocity of the unburnt mixture approaching the flame and  $\varphi/2$  denotes half of the flame angle. Figure 6 illustrates the method, how the turbulent flame speed is determined in experiments.

Using such an evaluation of the turbulent flame speed, the validation can also be interpreted as a rough comparison of the averaged flame shape and flame position. The database has been chosen since it allows to test the prediction of the model concerning flame shape and position via the turbulent flame speed for different turbulence levels and especially at

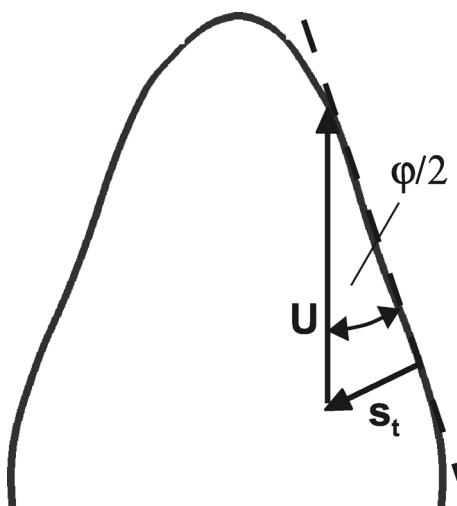


**Fig. 6** Method of determining the turbulent flame speed in experiment

different pressure levels. It might be argued, that a successful prediction of such an averaged global quantity using LES might be a fortunate combination of the applied model, numerics, mesh size and boundary conditions. However it is argued here, that such uncertainties are minimized by a successful simulation of different flames at a large number of different operation points on different mesh sizes and by a comparison of averaged and instantaneous predicted quantities.

## 4.2 Numerical setup

As for the 1-D simulation, the open source solver library OpenFOAM-1.6® is employed to perform the LES. 26 operation points from the Kobayashi database were simulated. The inlet and operating conditions for the combustion cases are listed in Table 1.

The global parameter ranges of the simulated cases, determined from these conditions, are summarised in Table 2, where the Zel'dovich flame thickness has been applied to determine  $Ka$  and  $Da$ .

As shown in Fig. 7, the location of the studied cases within the combustion regimes resulting from the BCs and ambient conditions are within the wrinkled, corrugated flamelet regime and thin reaction zone regimes.

The computational domain exhibits a diameter of 80 mm and length of 120 mm. Since the nozzle diameter is 20 mm and the maximum simulated flame length is about 50 mm, the simulation results are assumed not to be affected by the boundaries. The computational domain and the structure of the computational grid are illustrated in Fig. 8.

At the inlet for all variables except the pressure, Dirichlet boundary conditions are applied. To provide the turbulence intensity and the integral length scale determined in the measurements at the inlet, a turbulence generator according to Kempf et al. [34], which is based on a diffusion method, has been used. Random noise would be a poor representation of the turbulence, where the fluctuations are rapidly damped and the flow might quickly become laminar. Turbulence at the inlet is assumed to be homogeneous and isotropic. The turbulence generator has been successfully implemented and validated in previous work by Tangermann et al. [68]. The correct prediction of the specified  $u'$ -values has been verified in the whole inlet plane by evaluation of the computed Reynolds stresses at the inlet-patch. Since the turbulence generator is not divergence free, small pressure fluctuations arise in the first mesh cell behind the inlet due to the pressure based solver and pressure correction applied here. Therefore, the integral length scales and  $u'$ -values are additionally determined at the centerline, several cells downstream the inlet via autocorrelation. The autocorrelation supports the determined rms-values at the inlet patch, and indicate slightly underestimated integral length scales with a maximum deviation of about 9 %.  $k_{SGS}$  at the inlet has been determined applying  $(2c_k/c_e)\Delta^2|S_{ij}|^2$ , where  $c_k = 0.94$  and  $c_e = 1.048$  according to [23]. Temperature is set to  $T_0 = 300$  K at the inlet, Neumann BCs for  $T$  are applied at the other boundaries. Total pressure  $p_{t,0}$  is set at the outlet, allowing for back-flow at ambient conditions. The cell size is used as filter width. Following Weller et al. [73] a one-equation eddy-viscosity model as derived by Schumann [62] and supported by Fureby et al. [23] is solved for a subgrid kinetic energy  $k_{SGS}$ . The SGS velocity fluctuation is determined via:  $u'_\Delta = \sqrt{2/3k_{SGS}}$ . The performance of the one equation model has been successfully validated via simulating pipe, channel and free jet flows with and without passive scalar transport and comparing the LES results with DNS-data [35]. The computational domain, illustrated in Fig. 8, is discretized with hexaedrons which are concentrated in the region where the flame is stabilised. A structured mesh is used to minimise numerical diffusion. To check the mesh sensitivity of the simulation results, LES on three

**Table 1** Ambient and inlet conditions of the simulated operation points from Kobayashi database

	fuel	$\Phi$	$p[MPa]$	$U[m/s]$	$u'[m/s]$	$l_t[mm]$
1	$CH_4$	0.9	0.1	2.02	0.00	0
2	$CH_4$	0.9	0.1	2.02	0.10	1.8
3	$CH_4$	0.9	0.1	2.33	0.20	1.43
4	$CH_4$	0.9	0.1	2.42	0.33	1.4
5	$CH_4$	0.9	0.1	2.36	0.46	1.25
6	$CH_4$	0.9	0.5	2.05	0.09	0.83
7	$CH_4$	0.9	0.5	2.53	0.19	0.99
8	$CH_4$	0.9	0.5	3.38	0.61	1.15
9	$CH_4$	0.9	0.5	2.21	0.40	1.15
10	$CH_4$	0.9	1.0	2.6	0.09	1.05
11	$CH_4$	0.9	1.0	3.4	0.26	0.9
12	$CH_4$	0.9	1.0	2.11	0.36	1.1
13	$CH_4$	0.9	1.0	4.64	1.20	1.4
14	$CH_4$	0.9	1.0	3.57	0.85	1.2
15	$CH_4$	0.9	2.0	2.84	0.21	1.15
16	$CH_4$	0.9	2.0	3.22	0.73	1.15
17	$CH_4$	0.9	2.0	2.42	0.50	1.15
18	$CH_4$	0.9	2.0	2.87	0.61	1.15
19	$C_3H_8$	0.9	0.1	1.75	0.10	1.7
20	$C_3H_8$	0.9	0.1	1.25	0.21	1.05
21	$C_3H_8$	0.9	0.1	1.5	0.26	1.25
22	$C_3H_8$	0.9	0.1	1.75	0.35	1
23	$C_3H_8$	0.9	0.5	1.89	0.10	1.02
24	$C_3H_8$	0.9	0.5	2.17	0.15	1.05
25	$C_3H_8$	0.9	0.5	2.76	0.20	0.96
26	$C_3H_8$	0.9	0.5	3.51	0.63	1.2

systematically refined grids have been carried out. The largest filter width is chosen to stay below the integral length scale and therefore also within in the range of fractal flame folding. Table 3 summarises the characteristic mesh data, where  $\Delta$  denotes the averaged filter size of the region, where the flame is located.

**Table 2** Range of global classification numbers determined from inlet and ambient conditions of selected and simulated operation points of Kobayashi database

fuel	$Re \cdot 10^3$	$Re_t$	$Ka$	$Da$	$p[MPa]$	$u'/s_L$
$CH_4$	2.6 – 82	11 – 1100	0.03 – 3.4	10 – 120	0.1 – 2	0.3 – 11
$C_3H_8$	2.4 – 21	10 – 200	0.01 – 0.5	20 – 170	0.1 – 0.5	0.2 – 3

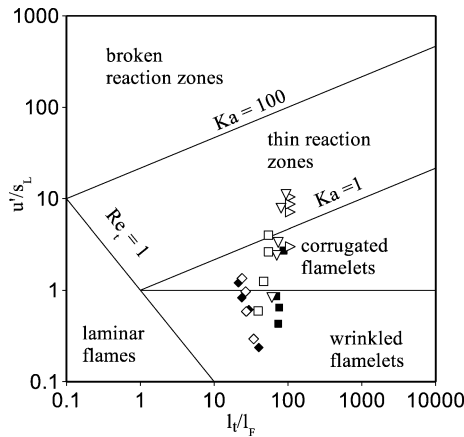


**Fig. 7** Investigated operation points in a regime diagram; methane: white; propane: black; 1 bar: diamonds; 5 bar: squares; 10 bar: triangles-down; 20 bar: triangles-right

Simulation and evaluation of results at each operation point is carried out as follows. For each combustion case, about 10 through flow times for flow development and additionally about 10 through flow times for time averaging are simulated. Circumferential averaging is applied to improve the statistics. The simulation time is e.g. about 8 h on 16 cores (2.0 GHz XEON processors) for case 1 with resolution A and about 4 h on 16 cores for case 8 with

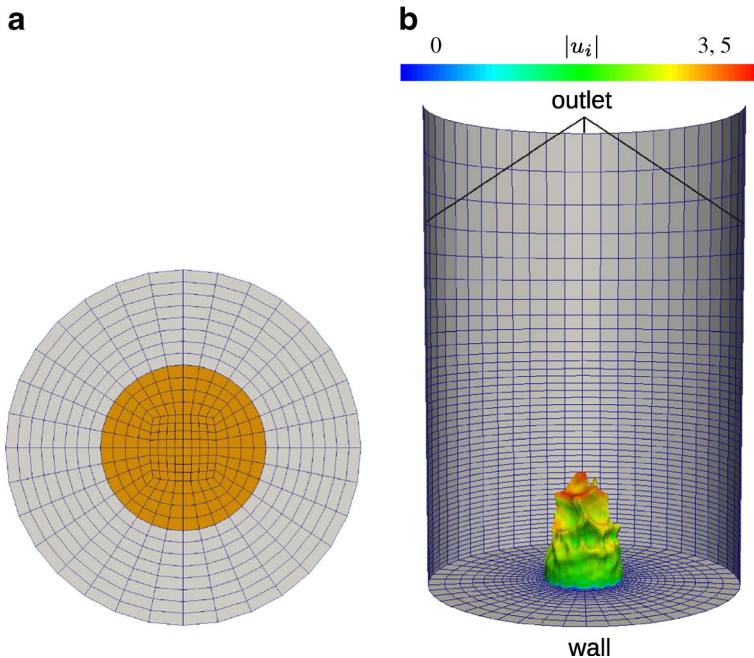


**Fig. 8** Simulation domain and boundaries for the simulated turbulent Bunsen flame, instantaneous flame front depicts position of the flame in the domain and distance to the boundaries; the mesh is strongly reduced for a clear representation

**Table 3** Mesh resolution and characteristics of the three investigated meshes

	$\Delta[mm]$	$n_{cells}$	$\frac{\Delta}{l_F} _{1bar}$	$\frac{\Delta}{l_F} _{5bar}$	$\frac{\Delta}{l_F} _{10bar}$	$\frac{\Delta}{l_F} _{20bar}$
A	0.4	$0.6 \cdot 10^6$	8.8	19	27.8	35.4
B	0.3	$2 \cdot 10^6$	6.6	14.2	20.9	26.6
C	0.2	$3.7 \cdot 10^6$	4.4	9.5	13.9	17.7

resolution A. As described above, the turbulent flame speed is extracted from measurements by determining the slope of an isoline which corresponds to  $\bar{c} = 0.5$ , neglecting the flame tip and the base region. Hence, the time and circumferentially averaged  $\bar{c}$  is used to compute a Reynolds averaged  $\bar{c}$  following [58] and assuming a BML model type flamelet FDF:

$$\bar{c} = \frac{(1 + \tau)\bar{c}}{1 + \tau\bar{c}} \quad (39)$$

where  $\tau = \rho_u/\rho_b - 1$  is the heat release factor. The slope of the isoline  $\bar{c} = 0.5$  is determined by a least squares fit neglecting the flame tip and base, here defined as the distance 10 % of the flame length from the flame tip and base. As illustrated in Fig. 6, the slope allows the computation of  $\varphi$ . With the bulk velocity  $U$  known at the inlet, the turbulent flame speed can be derived, see Eq. 38. The comparison of the turbulent flame speed can therefore be interpreted as a rough comparison of the predicted and measured flame shape and position.

### 4.3 Results and evaluation

#### 4.3.1 Assessment of LES quality

Assessment of the LES quality is provided by an evaluation of the ratio of the resolved turbulent kinetic energy  $k_{res}$  to the total turbulent kinetic energy  $k_{tot} = k_{SGS} + k_{res}$ . This is shown in Fig. 9 for case 5 and 16 for mesh resolutions A and C evaluated on the center line.

About 85–90 % of the turbulent kinetic energy for resolution A is resolved. At a nozzle distance of about  $x = 1 \text{ cm}$  the combustion process starts and the resolved kinetic energy is superimposed by the intermittency of the computed flame [58]. Hence, the LES quality is evaluated only in the unburned region. A more sophisticated evaluation of LES quality has been proposed by Celik et al. [8] by suggesting a model that accounts for the contribution of numerical turbulent kinetic energy to  $k_{tot}$ . The method has already been applied in the

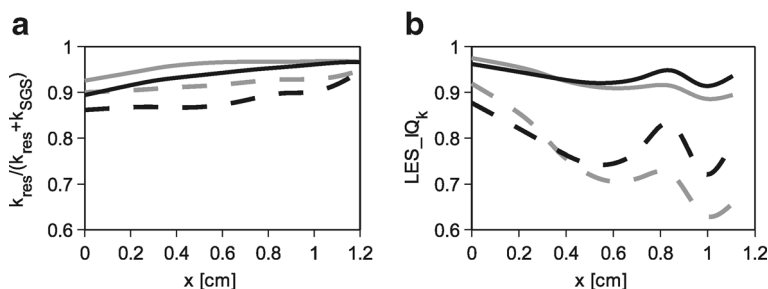


**Fig. 9** **a** Ratio of resolved turbulent kinetic energy to total turbulent kinetic energy for case 5 and 16 at two different mesh sizes; **b** Ratio of resolved turbulent kinetic energy to total turbulent kinetic energy including numerical turbulent kinetic energy applying (40); case 5A: black dashed; case 5C: black solid; case 16A: grey dashed; case 16C: grey solid

context of premixed combustion by Aluri et al. [1]. An index for the LES quality is defined by

$$LES\_IQ_k = \frac{k_{res}}{k_{tot}} = \frac{k_{res}}{k_{res} + a_k h^p} \quad (40)$$

where  $a_k h^p$  denotes an effective SGS turbulent kinetic energy.  $h$  denotes the mesh size,  $p$  the order of discretization, here approximated by a value of 2 and  $a_k$  is a coefficient defined as:

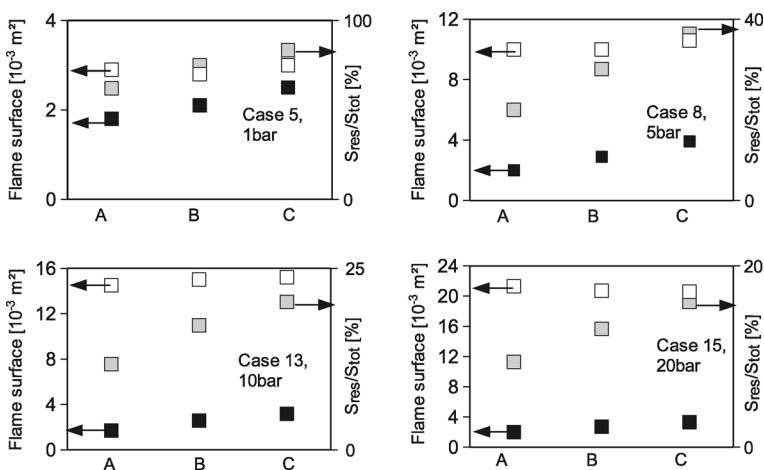
$$a_k = \frac{1}{h_{fine}^p} \left[ \frac{k_{res,fine} - k_{res,rough}}{(k_{res,rough}/k_{res,fine})^p - 1} \right] \quad (41)$$

Figure 9b shows the distribution of  $LES\_IQ_k$  on the center line of case 5 and 16 for the isothermal range. At the inlet Fig. 9a, b predict similar values. Further downstream, Eq. 40 predicts a ratio of  $k_{res}$  to  $k_{tot}$  of about 0.65–0.8 for case A. In [8], a good LES is characterised by a rate of 0.7–0.8 of resolved turbulent kinetic energy, which is achieved in case 5 and almost achieved in case 16 for coarsest resolution A.

#### 4.3.2 Evaluation of the combustion model

To evaluate the model properties at different pressure levels, the cases 5, 8, 14, 16, in Table 1 are chosen. Pressure varies between  $0.1 \text{ MPa} \leq p \leq 2 \text{ MPa}$ , the integral length scale is about  $1.2 \text{ mm}$ . The turbulence intensity  $I$  varies between  $19 \% \leq I \leq 22 \%$  and the  $u'/s_L^0$ -values are  $1.3|_{0.1 \text{ MPa}}$ ,  $3.9|_{0.5 \text{ MPa}}$ ,  $7.7|_{1 \text{ MPa}}$  and  $10|_{2 \text{ MPa}}$ . Cases 5, 8, 14 and 16, see Table 1, are evaluated concerning the resolved and total flame surface in Fig. 10. The total flame surface is computed via,  $S_{tot} = \int_{\Omega} \Sigma \, dV$ , the resolved flame surface is computed via,  $S_{res} = \int_{\Omega} |\nabla \tilde{c}| \, dV$

Considering the 1bar case the ratio of total to resolved flame surface increases from about 50 % to 80 % with increasing resolution. Thus, all 1 bar cases 1 – 5 correspond to a highly resolved flame surface. With increasing pressure, the influence of SGS wrinkling increases. Although at 20 bar at least for resolution C about 90 % of turbulent kinetic energy is resolved, only 15 % of the flame surface is resolved. Similar  $S_{res}/S_{tot}$ -values with varying



**Fig. 10** Evaluation of resolved flame surface (black symbol) and total surface (white symbol) and  $S_{res}/S_{tot}[\%]$  (grey symbol) for filter width A,B,C see Table 3 and cases 5,8,14,16 see Table 1



pressure are predicted by Richard et al. [60] via LES of a real internal combustion engine configuration. Thus at moderate to high Reynolds number combustion, despite a highly resolved flow field LES, the main part of flame surface or reaction rate is on *SGS* level. To illustrate the influence of mesh resolution on the computed flame surface and the spatial distribution of total and resolved flame surface, further model evaluations are carried out using case 5 and case 16. The instantaneous flame, evaluated at  $\tilde{c} = 0.5$ , for case 5 and 16 with filter size A and C is shown in Fig. 11.

Pressure influence on the resolved flame wrinkling is not visible in the simulations, whereas the experimental data in [39–41] shows a distinct pressure influence on the flame surface. Using a smaller cell size/filter width a more wrinkled flame is computed. According to the regime diagram in Fig. 7, case 5 is within the corrugated flamelet regime and case 16 is in the thin reaction zone regime. The combustion regime diagram proposed by Pitsch [57] can be used to classify the considered cases in LES context. The LES diagram shown in Fig. 12 is modified compared to the one proposed by Pitsch [57] in such a manner, that the Gibson scale  $l_G \sim Ka^{-2}$  is not applied to model the inner cut-off scale and therefore does not describe the boundary between corrugated regime and resolved flame surface. Here, the inner cut-off is defined as  $\epsilon_i = l_F Ka_{\Delta}^{-1/2}$  which corresponds to the line  $Re_{\Delta} = 1$  using  $Re_{\Delta} = u'_{\Delta} \Delta / s_L^0 l_F$  and defines the boundary to resolved flame wrinkling.  $Ka_{\Delta}$  and  $\Delta / l_F$  are evaluated on an instantaneous flame surface defined here as  $\tilde{c} = 0.5$ . The three different resolution levels A, B and C are evaluated. As shown in Fig. 12, single operation points in Fig. 7 expand into a range of points in LES context.

The Karlovitz number  $Ka_{\Delta} = (u'_{\Delta} / s_L^0)^{3/2} (\Delta / l_F)^{-1/2}$  is approximately independent on  $\Delta$  within the inertial range, but varies along the flame due to decay of turbulence. Fig. 12 shows, that the range of computed  $Ka_{\Delta}$  numbers is similar for different mesh resolutions. Consistent with the findings in Fig. 10, case 5B and 5C represent cases with rather well resolved flame surface. In contrast to the classification of case 16 to the thin reaction zone regime in Fig. 7, in the LES context case 16 mainly belongs to the corrugated flamelet regime. Figure 13 shows the effect of mesh refinement on the time averaged progress variable  $\langle \bar{c} \rangle$  and the instantaneous Favre filtered progress variable  $\tilde{c}$  for the 1 bar cases 5A and 5C, where 60–80 % of the flame surface is resolved. To investigate flames with larger model influence, Fig. 14 shows the spatial distribution of  $\langle \bar{c} \rangle$  and  $\tilde{c}$  for case 16A and 16C which corresponds to a model contribution to the total flame surface of about 9–16 % when moving from case 16A to case 16C.  $\tilde{c}$  is displayed, since it is the variable which is solved in Eq. 2 while  $\langle \bar{c} \rangle$  is the variable which is used for comparison with experimental data. The grid properties of cases A, C are summarised in Table 3.

Downstream of the inlet region, the instantaneous turbulent flame is resolved by about 6 cells for mesh resolutions A and C. A smoother resolved flame surface for the coarsest

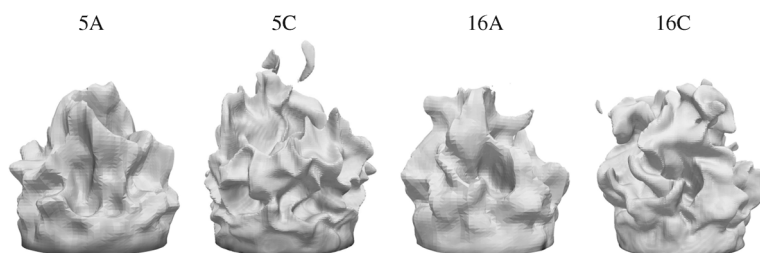


**Fig. 11** Influence of filter width and pressure on the instantaneous 3D flame front, for case 5 and 16, using filter width A and C, compare Table 1 and 3

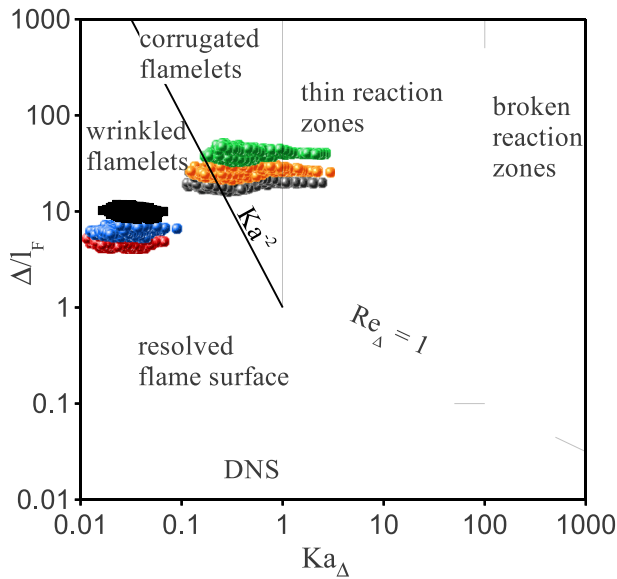


**Fig. 12** LES-Regime diagram for the investigated Bunsen flame case 5 and 16 and filter width A, B, C; 5A: black; 5B: blue; 5C: red; 16A: green; 16B: orange; 16C: grey

mesh size and more strongly wrinkled resolved flame surfaces on finer grids are predicted with increasing mesh resolution. Although the instantaneous turbulent flame brush is thinner comparing case C to case A, the time averaged turbulent flame flame brush is not influenced

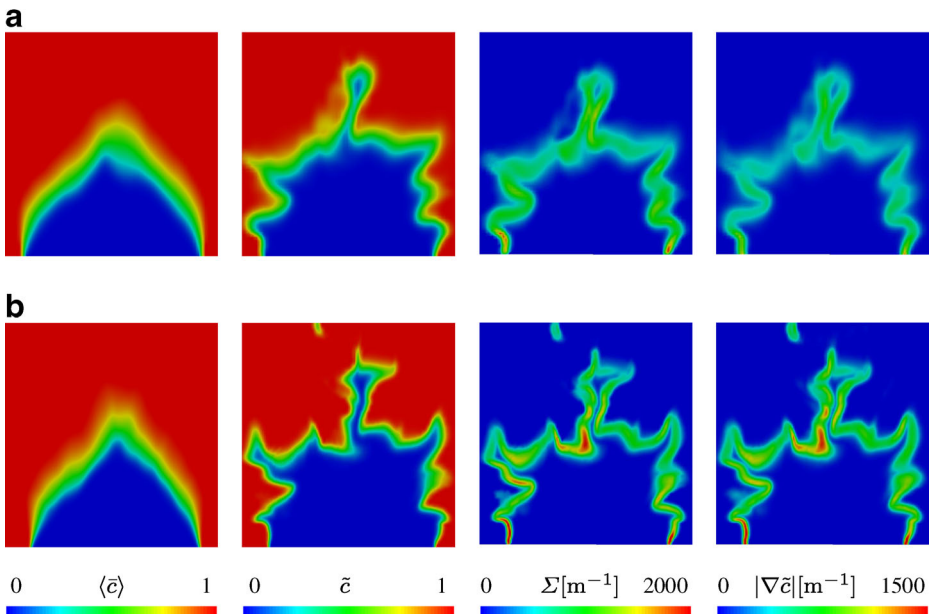


**Fig. 13** Influence of filter width on the time averaged  $\langle \bar{c} \rangle$  and the instantaneous flame surface  $\tilde{c}$ , the FSD  $\Sigma$  and  $|\nabla \tilde{c}|$ ; **a** case 5A ; **b** case 5C, compare Tables 1 and 3

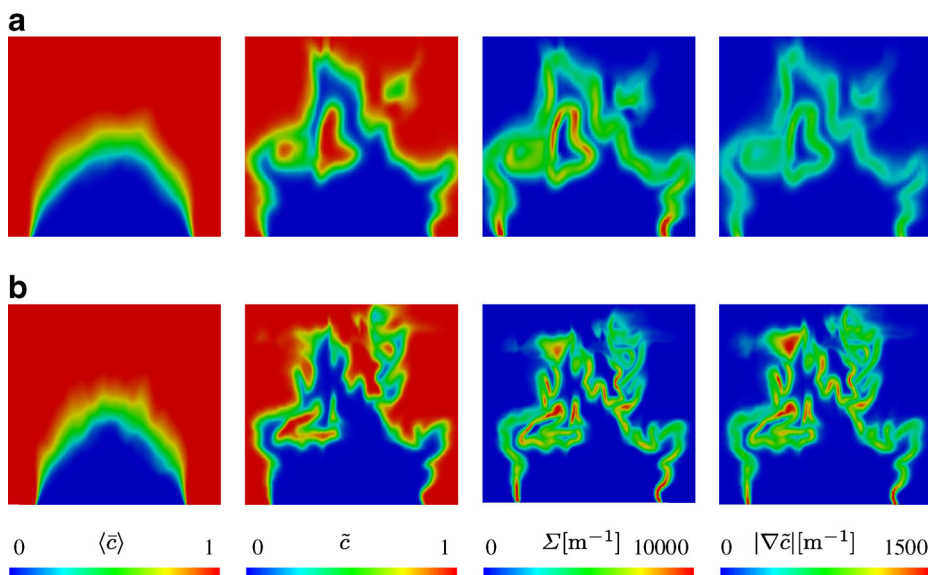


**Fig. 14** Influence of filter width on the time averaged  $\langle \tilde{c} \rangle$  and the instantaneous flame surface  $\tilde{c}$ , the FSD  $\Sigma$  and  $|\nabla \tilde{c}|$ ; **a** case 16A ; **b** case 16C, compare Tables 1 and 3

much by an increasing mesh resolution. Figure 13 for case 5 and Fig. 14 for case 16 illustrate the influence of mesh resolution on the spatial distribution on the total FSD and on  $|\nabla \tilde{c}|$  which is considered here as an indicator for the resolved flame surface since it is directly incorporated into the reaction rate.

Comparing the magnitudes of  $\Sigma$  and  $|\nabla \tilde{c}|$  confirms that cases 5A and 5C represent a highly resolved flame surface as already shown in Fig. 10. The increased mesh resolution produces larger gradients of the progress variable since a thinner and a more strongly wrinkled instantaneous turbulent flame brush is predicted, compared to a smoother surface for resolution A. Differences in magnitude of  $|\nabla \tilde{c}|$  are compensated by an increased influence of the SGS flame wrinkling model for the coarser resolution. Additionally for resolution A, the distribution of  $\Sigma$  (normal to the flame surface) is more smeared and broadened compared to the refined case C. The combination of increased model contribution and broadened instantaneous flame brush thickness with decreasing mesh resolution finally leads to a predicted total flame surface, which depends weakly on mesh resolution. To investigate whether the same observations are valid for predicted flames with large model contribution, Fig. 14 illustrates the same model evaluation for 2 MPa, case 16. The magnitudes of  $|\nabla \tilde{c}|$  and  $\Sigma$  differ by one order in magnitude, showing that about 10 % of the flame surface is resolved. The slightly increased values of  $|\nabla \tilde{c}|$  compared to case 5 in Fig. 13 are due to the increased rms-values at the inlet for case 16. Nevertheless, the same observations for case 16 as for case 5 are valid. The distributions of the FSD and  $|\nabla \tilde{c}|$  are more highly resolved with increasing mesh resolution and despite of large differences in instantaneous  $|\nabla \tilde{c}|$  for the different resolutions, values of total  $\Sigma$  are balanced due to the SGS wrinkling model. The predicted constant total flame surface with decreasing mesh resolution is due to an increased influence of the SGS flame wrinkling model but also due to a broadened spatial range of the reaction rate. Comparing the instantaneous flame front in

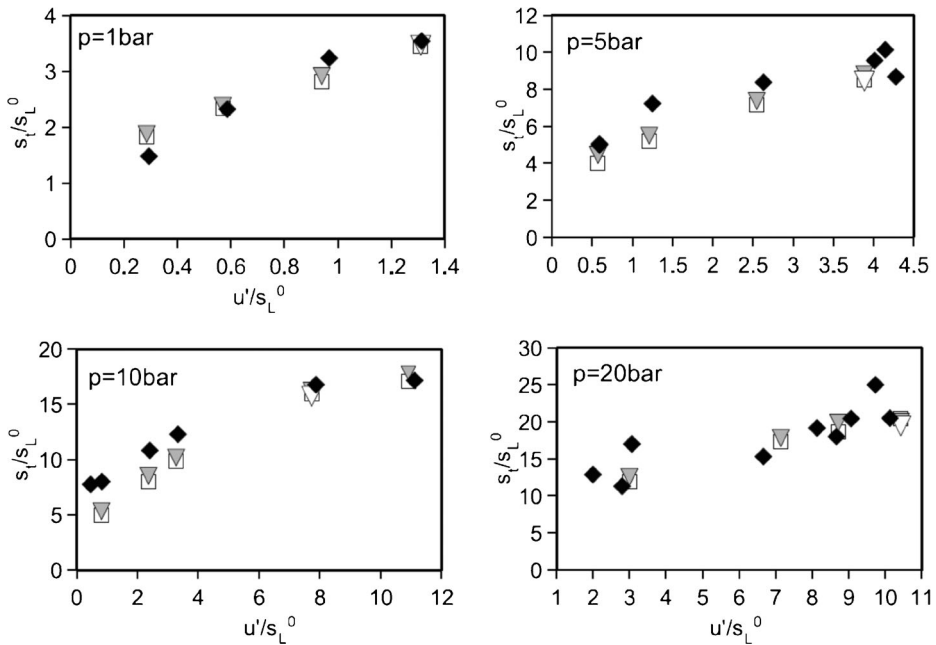


**Fig. 15** Comparison of  $s_t$  evaluated from simulation for 3 different mesh sizes with experimental data for methane fuel; experimental data: black diamonds; case a grey triangles; case b white squares; case c white triangles

Figs. 13 and 14 shows, that despite the pressure increase from 1 bar - 20 bar, where experimental data shows an highly increased wrinkling of the flame front, the resolved wrinkling in the LES stays nearly constant.

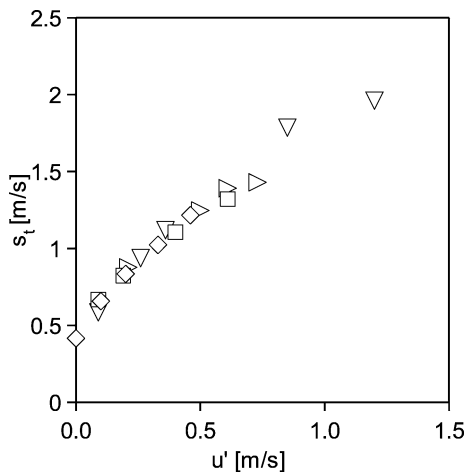


**Fig. 16** Predicted turbulent flame speed using mesh resolution A at 4 different pressure levels for methane,  $\Phi = 0.9$ ; 1 bar: diamonds; 5 bar: squares; 10 bar: triangles down; 20 bar: triangles right

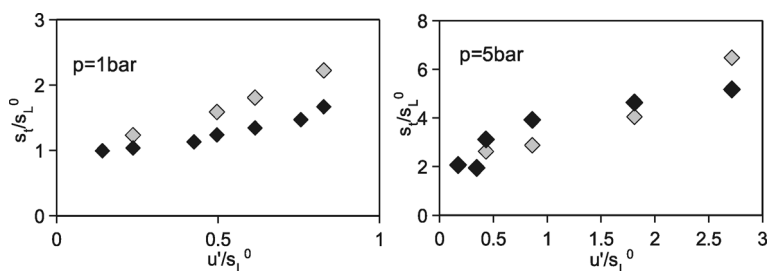


**Fig. 17** Comparison of  $s_t$  evaluated from simulation for mesh resolution A with experimental data for propane fuel; experimental data: black diamonds; simulation: grey diamonds

#### 4.3.3 Comparison with experimental results

The comparison of simulation results for the three different mesh sizes and experimental data in terms of turbulent flame speed for methane as fuel is presented in Fig. 15. Due to the larger computational cost using the finest mesh (case C in Table 3) only one case per pressure level has been simulated at this resolution.

The simulation results applying (28) as combustion model correctly reproduce trends of the turbulent flame speed over a large range of pressure and turbulence levels without adaption of model constants. Only for 10 bar at low turbulence levels the predicted turbulent flame speed slightly underestimates the measured flame speed. Figure 15 also shows, that the predicted global turbulent flame speed is nearly independent of the mesh size, for the resolution levels considered here.

As argued in Section 2, experimental data from the PSI rig by Griebel et al. [28] and experimental data summarised in [49] suggest, that for methane, the turbulent flame speed is independent of the pressure. The predicted  $s_t$  is plotted versus  $u'$  in Fig. 16 to check, whether the proposed model can match this experimental finding.

The simulated  $s_t$  for different pressure levels indeed fall on a single line. Simulations using propane fuel have been carried out to investigate the combustion model performance using a second fuel. Propane exhibits a Lewis number of about  $Le \approx 1.64$  and slight Lewis number effects are expected. A Lewis number larger than one denotes a faster diffusion of heat away from the flame front compared to species diffusion, which might result in a reduced flame speed. Figure 17 displays the comparison of simulation results and experimental data for propane fuel.

For 1 bar and up to  $u'/s_L^0 = 0.25$  the predicted turbulent flame speed matches the experimental data. With increasing turbulence level, deviations arise and the turbulent flame speed is increasingly over predicted. However, the pressure scaling is predicted very well. Within a turbulence level range  $0 < u'/s_L^0 < 2$  the predicted turbulent flame speed matches the experimental data very well at  $p = 5$  bar.

**Table 4** Ambient and inlet conditions and global classification numbers of the simulated of the simulated operation points from the PSI rig

Fall	$p[MPa]$	$\Phi$	$u'[m/s]$	$l_t[mm]$	$T_u[K]$	$Da$	$Ka$	$Re_d$	$Re_t$
1	0.1	0.5	3.2	2.5	673	3	3	$16, 1 \cdot 10^3$	130
2	0.5	0.5	3.2	2.5	673	3.5	8	$80, 6 \cdot 10^3$	653

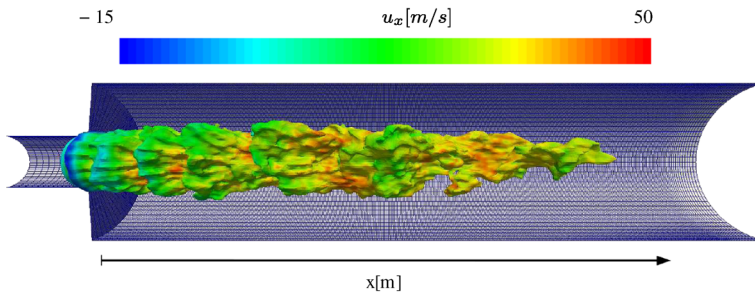


**Fig. 18** PSI flame: computational domain with instantaneous flame front, contour shows axial velocity

## 5 Simulation of a Turbulent Jet Flame

To evaluate the combustion model in terms of a complete flame shape and the flow field, the Paul Scherrer Instituts (PSI) burner, which represents a highly turbulent jet flame, is simulated. Flame shape and experimental data are taken from Griebel et al. [28] and Siewert [64], the experimental flow field has been taken from [19]. The PSI rig, representing combustion regimes typical for stationary gas turbines, has already been simulated by Durand [19] and Duwig et al. [20] in the LES context.

### 5.1 Experimental setup

The combustion takes place in a high pressure chamber, with a length of 320 mm and a diameter of 75 mm. The PSI rig can be operated at pressure levels up to 30 bar and a maximum thermal power of about 400 kW. A turbulence grid upstream of the inlet nozzle (diameter 25 mm) allows to adjust the turbulence level. PIV is used to investigate the flow field, OH-PLIF is used to measure the flame front. An averaged flame front is determined by averaging 800 pictures of the instantaneous binarized flame front.

### 5.2 Numerical setup

The chosen inlet and operation conditions for the simulated operation points are listed in Table 4.

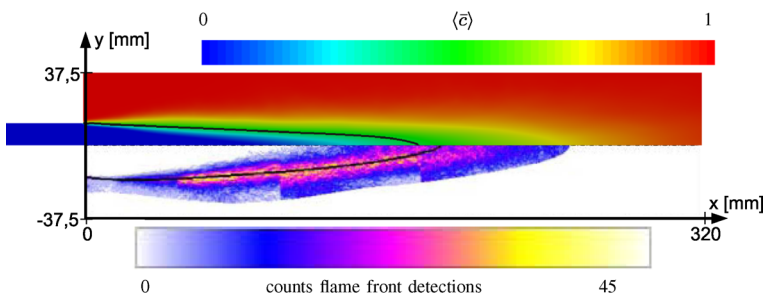


**Fig. 19** Comparison of averaged flame front for 5 bar, black line corresponds to  $\langle \bar{c} \rangle = 0.5$

As described in Section 4.2, the turbulence generator following Kempf et al. [34] is applied to allow a reasonable flow field at the inlet. The computational domain is shown in Fig. 18.

The combustion chamber in axial, radial and circumferential direction has been discretized with  $366 \times 75 \times 80$  hexahedrons. The pipe upstream of the combustion chamber,

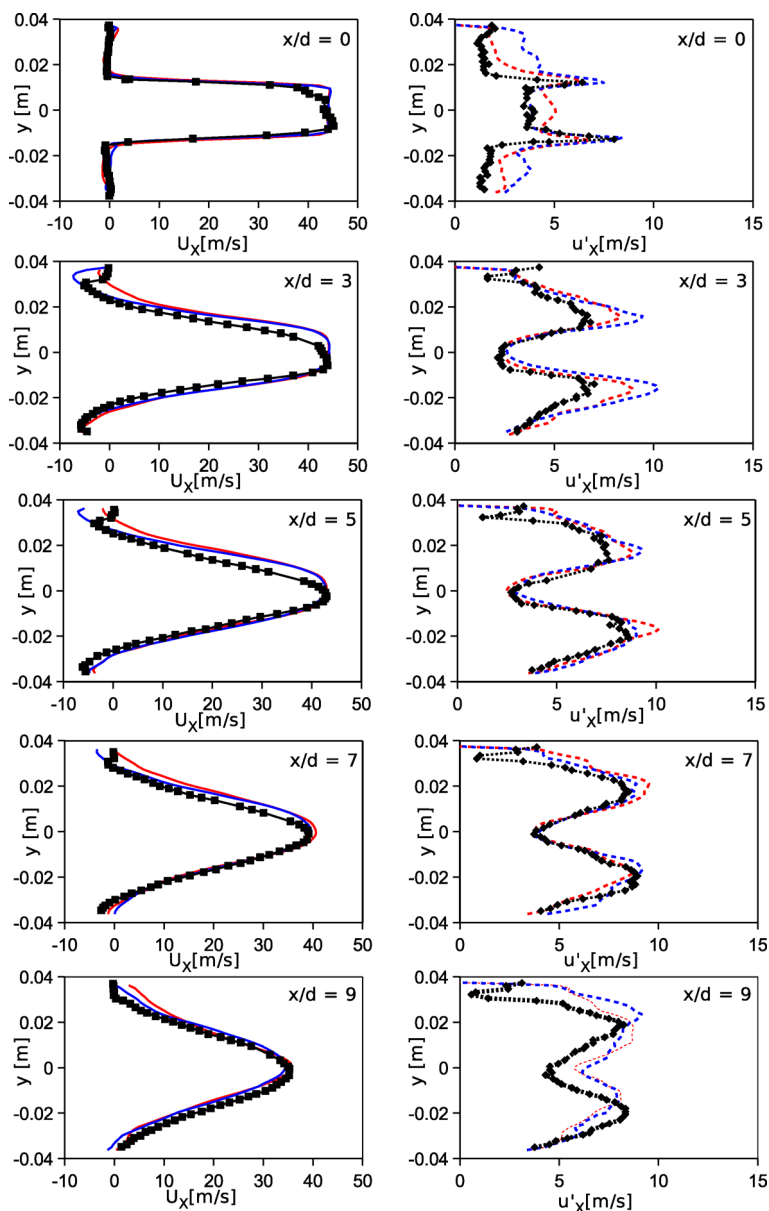


**Fig. 20** Comparison of the axial velocity and the axial fluctuation for LES and experiment at 5 position in the combustion chamber; experiment (black), LES 5 bar (blue), LES 1 bar (red)

with a length of 30 mm is discretized with  $21 \times 25 \times 80$  hexahedrons. About 10 flow through times are simulated to obtain a developed flow field and additional 10 flow through times are simulated for time averaging.

### 5.3 Comparison with experimental data

The comparison of the simulated flame front with experimental data is shown in Fig. 19.

The length of the iso line  $\langle \bar{c} \rangle = 0.5$  very slightly underestimates the flame front in the experiment. The flame shape in terms of the growth of flame brush with distance from the nozzle exit is in a quite good agreement with the experimental data. The comparison of the axial velocity and the axial fluctuation of simulation and experiment is shown in Fig. 20.

Experimental data in [20] indicate a minor influence of pressure on the flow field. To investigate the pressure dependence predicted by the combustion model, LES at 1 bar and 5 bar are performed. At  $y < 0$  the simulated flow field matches the experimental data, while at  $y > 0$ , due to an asymmetry of the experimental data, slight deviations arise. The comparison of the velocity fields for both LES results show a slightly increased entrainment at 1 bar. Despite of that, the experimental and LES flow fields can be regarded to be nearly identical. Comparing the field of the turbulent fluctuation  $u'$ , one has to bear in mind, that besides the turbulent eddy fluctuations the flow field is influenced by the intermittency of the turbulent flame. Hence  $u'$  does not only represent the turbulent eddy fluctuation but contains additional contributions from the intermittency [58]. The evaluation method in experiment and simulation however is similar, allowing a direct comparison of  $u'$  data. At  $x/d = 3$ , the LES overestimates the peak of the experimental velocity fluctuation, while the core flow follows the experimental data. This might indicate that the beginning of the combustion process in the simulation is predicted a bit more upstream compared to the experiment. While near the flame base experimental data and LES results are in a good agreement, at  $x/d = 9$  the slightly longer flame in the simulation causes some deviations. Like for the velocity field, the simulation data for 1 bar and 5 bar matches well and supports the pressure independence of turbulent methane combustion. Deviations arise only at  $x/d = 3$ . Note that no model parameters were adjusted for simulation of the PSI configurations.

## 6 Conclusions

A scalar LES SGS flame surface density model for premixed combustion has been derived, based on the physical concepts of the RANS closure approach for fractal wrinkling of flamelets proposed by Gouldin et al. [27], which is extended here into the low Re range and taking into account effects of flame stretch on the local laminar flame speed. The assumption of fractal characteristics of the flame surface requires a suitable formulation of the inner cut off scale and the fractal dimension. Based on experimental and DNS databases, summarised in Gülder and Smallwood [29] and the experimental database of Kobayashi et al. [42], the inner cut off scale has been chosen to scale  $\epsilon_i \sim Ka_\Delta^{-1/2}$ , uniform for the wrinkled, corrugated flamelet regime and the thin reaction zone regime. For the fractal dimension  $D$ , a function dependent on  $Ka_\Delta$  is proposed, which fits the theoretical model for  $D$  proposed by Giacomazzi et al. [7]. To model strain effects on the laminar flame speed, the linear theory of instabilities is used. The principal characteristics of the FSD model in the LES context are evaluated in 1-D simulations. The model predicts a reasonable increase of SGS flame wrinkling and the turbulent flame speed with increasing turbulence intensity and reduces to the laminar flame speed in the limit of zero turbulence. A turbulent Bunsen flame, using



the database of Kobayashi et al. [39–41], which provides measured turbulent flame speeds for low and moderate turbulence intensity at pressure levels 0.1 MPa, 0.5 MPa, 1.0 MPa, 2.0 MPa and 3.0 MPa has been chosen to evaluate further model characteristics. Four operation points in the range 0.1 MPa–2.0 MPa are simulated on three different mesh resolutions to show the mesh independence of the total flame surface and the effect of mesh resolution on resolved and subgrid scale flame wrinkling. Simulation results and experimental data of 25 operation points are compared in terms of the turbulent flame speed which has been determined via an equivalent evaluation method in experiment and simulation. Using methane fuel, the predicted turbulent flame speeds match the experimental data very well in the whole range from low to high turbulence levels. Simulations of the operation points on 2–3 different mesh resolutions exhibit a mesh independence of the predicted averaged turbulent flame speed. The independence of the turbulent flame speed on pressure for methane fuel suggested by experimental databases is reproduced by the model. Slight overestimations of  $s_t$  are predicted using propane fuel at 1 bar while at 5 bar and a turbulence level  $0.25 < u'/s_L^0 < 2$  the trends of the experimental data can be predicted very well. A turbulent jet flame, experimentally investigated by Griebel et al. [28] is simulated to assess the combustion model in terms of flame shape, velocity and turbulence field. The simulated flame shape matches the experimental one quite well and overestimates only slightly the turbulent flame thickness at the flame tip. The field of the axial velocity is in a very good agreement with experimental data and the turbulent fluctuations can reproduce the trends of the turbulence field in the experiments. In conclusion, a model is proposed for the simulation of turbulent premixed flames in the LES context. It is based on physical arguments, is valid from zero to high turbulence intensity, correctly scales with pressure and is relatively insensitive to filter size.

## References

- Aluri, N., Muppala, S., Dinkelacker, F.: Large Eddy Simulation of lean premixed turbulent flames of three different combustion configurations using a novel reaction closure. *Flow Turbul. Combust.* **80**, 207–224 (2008)
- Boger, M., Veynante, D.: Large Eddy Simulations of a turbulent premixed v-shaped flame. *Adv. Turbul.* **VIII** (2000)
- Boger, M., Veynante, D., Boughanem, H., Trouvé, A.: Direct numerical Simulation analysis of flame surface density concept for Large Eddy Simulation of turbulent premixed combustion. *Symp. Int. Combust.* **27**(1), 917–925 (1998)
- Brandl, A., Pfitzner, M., Mooney, J., Durst, B., Kern, W.: Comparison of combustion models and assessment of their applicability to the simulation of premixed turbulent combustion in SI-engines. *Flow Turbul. Combust.* **75**, 335–350 (2005)
- Bray, K.N.C., Champion, M., Libby, P.: Pre-mixed flames in stagnating turbulence: part V—evaluation of models for the chemical source term. *Combust. Flame* **127**, 2023–2040 (2001)
- Bronstein, I., Semendjajew, K., Musiol, G., Mühlig, H.: *Taschenbuch der Mathematik*. Harry Deutsch (2008)
- Bruno, E., Favini, C., Giacomazzi, B.: Fractal modeling of turbulent combustion. *Combust. Theory Model.* **4**(4), 391–412 (2000)
- Celik, I.B., Cehreli, Z.N., Yavuz, I.: Index of resolution quality for Large Eddy Simulations. *J. Fluids Eng.* **127**(5), 949–958 (2005)
- Chakraborty, N., Cant, R.: Effects of Lewis number on flame surface density transport in turbulent premixed combustion. *Combust. Flame* **158**(9), 1768–1787 (2011)
- Chakraborty, N., Klein, M.: A priori direct numerical simulation assessment of algebraic flame surface density models for turbulent premixed flames in the context of Large Eddy Simulation. *Phys. Fluids.* **20**(8), 085,108 (2008)

11. Charlette, F., Meneveau, C., Veynante, D.: A power-law flame wrinkling model for LES of premixed turbulent combustion Part I: non-dynamic formulation and initial tests. *Combust. Flame* **131**(1–2), 159–180 (2002)
12. Charlette, F., Meneveau, C., Veynante, D.: A power-law flame wrinkling model for LES of premixed turbulent combustion Part II: dynamic formulation. *Combust. Flame* **131**(1–2), 181–197 (2002)
13. Clavin, P.: Dynamic behavior of premixed flame fronts in laminar and turbulent flows. *Prog. Energy Combust. Sci.* **11**(1), 1–59 (1985)
14. Colin, O., Ducros, F., Veynante, D., Poinso, T.: A thickened flame model for Large Eddy Simulations of turbulent premixed combustion. *Phys. Fluids*. **12**(7), 1843–1863 (2000)
15. Constantin, P., Procaccia, I., Sreenivasan, K.: Fractal geometry of isoscalar surfaces in turbulence: theory and experiments. *Phys. Rev. Lett.* **67**, 1739–1743 (1991)
16. Das, A.: A fractal analysis of premixed turbulent flames. PhD thesis, University of British Columbia (1993)
17. Dinkelacker, F., Hölzler, S.: Investigation of a turbulent flame speed closure approach for premixed flame calculations. *Combust. Sci. Technol.* **158**(1), 321–340 (2000)
18. Driscoll, J.F.: Turbulent premixed combustion: Flamelet structure and its effect on turbulent burning velocities. *Prog. Energy Combust. Sci.* **34**(1), 91–134 (2008)
19. Durand, L.: Development, implementation and validation of LES models for inhomogeneously premixed turbulent combustion. Dissertation, Technische Universität München (2007)
20. Duwig, C., Fuchs, L., Griebel, P., Siewert, P., Boschek, W.: Study of a confined turbulent jet: influence of combustion and pressure. *AIAA J.* **45**(3), 624–639 (2007)
21. Ferziger, J.H., Echehki, T.: A simplified reaction rate model and its application to the analysis of premixed flames. *Combust. Sci. Technol.* **89**(5–6), 293–315 (1993)
22. Fureby, C.: A fractal flame-wrinkling Large Eddy Simulation model for premixed turbulent combustion. *Proc. Combust. Inst.* **30**(1), 593–601 (2005)
23. Fureby, C., Tabor, G., Weller, H.G., Gosman, A.D.: A comparative study of subgrid scale models in homogeneous isotropic turbulence. *Phys. Fluids*. **9**(5), 1416–1429 (1997)
24. Goix, P.J., Shepherd, I.G., Trinite, M.: A fractal study of a premixed V-shaped H<sub>2</sub>/Air flame. *Combust. Sci. Technol.* **63**(4–6), 275–286 (1989)
25. Göttgens, J., Mauss, F., Peters, N.: Analytic approximations of burning velocities and flame thicknesses of lean hydrogen, methane, ethylene, ethane, acetylene, and propane flames. Twenty-Fourth Symposium on Combustion. *Symp. Int. Combust.* **24**(1), 129–135 (1992)
26. Gouldin, F.: An application of fractals to modeling premixed turbulent flames. *Combust. Flame* **68**(3), 249–266 (1987)
27. Gouldin, F., Bray, K., Chen, J.Y.: Chemical closure model for fractal flamelets. *Combust. Flame* **77**(3–4), 241–259 (1989)
28. Griebel, P., Bombach, R., Inauen, A., Scharen, R., Schenker, S., Siewert, P.: Flame characteristics and turbulent flame speeds of turbulent, high-pressure, lean premixed methane/air flames. *ASME Conference Proceedings* 2005(4725X), 405–413 (2005)
29. Gülder, Ö.L., Smallwood, G.J.: Inner cutoff scale of flame surface wrinkling in turbulent premixed flames. *Combust. Flame* **103**(1–2), 107–114 (1995)
30. Hawkes, E.R., Cant, R.S.: Implications of a flame surface density approach to Large Eddy Simulation of premixed turbulent combustion. *Combust. Flame* **126**(3), 1617–1629 (2001)
31. Hawkes, E.R., Chatakonda, O., Kolla, H., Kerstein, A.R., Chen, J.H.: A petascale direct numerical simulation study of the modelling of flame wrinkling for Large Eddy Simulations in intense turbulence. *Combust. Flame* **159**(8), 2690–2703 (2012)
32. Hernández-Pérez, F., Yuen, F., Groth, C., Gülder, Ö.: LES of a laboratory-scale turbulent premixed Bunsen flame using FSD, PCM-FPI and thickened flame models. *Proc. Combust. Inst.* **33**(1), 1365–1371 (2011)
33. Jasak, H.: Error Analysis and Estimation for the Finite Volume Method with Applications to Fluid Flows. PhD thesis, Imperial College of Science, Technology and Medicine (1996)
34. Kempf, A., Klein, M., Janicka, J.: Efficient generation of initial- and inflow-conditions for transient turbulent flows in arbitrary geometries. *Flow Turbul. Combust.* **74**, 67–84 (2005)
35. Keppeler, R., Kranawetvogl, J., Jarczyk, M.M., Pfitzner, M.: Large Eddy Simulationen von Rohr- Kanal- und Freistrahlsströmung mit OpenFOAM. Technical report, Universität der Bundeswehr München (2011)
36. Keppeler, R., Tangermann, E., Pfitzner, M.: Extension of a Large Eddy Simulation combustion model for high pressures and for low Reynolds number flames. *Proceedings of European Combustion Meeting*, Cardiff (2011)
37. Kerstein, A.R.: Fractal dimension of turbulent premixed flames. *Combust. Sci. Technol.* **60**(4–6), 441–445 (1988)

38. Klimenko, A.Y.: Examining the cascade hypothesis for turbulent premixed combustion. *Combust. Sci. Technol.* **139**, 15–40 (1998)
39. Kobayashi, H., Tamura, T., Maruta, K., Niioka, T., Williams, F.A.: Burning velocity of turbulent premixed flames in a high-pressure environment. *Symp. Int. Combust.* **26**(1), 389–396 (1996)
40. Kobayashi, H., Nakashima, T., Tamura, T., Maruta, K., Niioka, T.: Turbulence measurements and observations of turbulent premixed flames at elevated pressures up to 3.0 MPa. *Combust. Flame* **108**(1–2), 104–110 (1997)
41. Kobayashi, H., Kawabata, Y., Maruta, K.: Experimental study on general correlation of turbulent burning velocity at high pressure. *Symp. Int. Combust.* **27**(1), 941–948 (1998)
42. Kobayashi, H., Kawazoe, H.: Flame instability effects on the smallest wrinkling scale and burning velocity of high-pressure turbulent premixed flames. *Proc. Combust. Inst.* **28**(1), 375–382 (2000)
43. Kuenne, G., Ketelheun, A., Janicka, J.: LES modeling of premixed combustion using a thickened flame approach coupled with FGM tabulated chemistry. *Combust. Flame* **158**(9), 1750–1767 (2011)
44. Lecocq, G., Richard, S., Colin, O., Vervisch, L.: Gradient and counter-gradient modeling in premixed flames: Theoretical study and application to the LES of a lean premixed turbulent swirl-burner. *Combust. Sci. Technol.* **182**(4–6), 465–479 (2010)
45. Lecocq, G., Richard, S., Colin, O., Vervisch, L.: Hybrid presumed pdf and flame surface density approaches for Large Eddy Simulation of premixed turbulent combustion: part I: formalism and simulation of a quasi-steady burner. *Combust. Flame* **158**(6), 1201–1214 (2011)
46. Lee, G.G., Huh, K.Y., Kobayashi, H.: Measurement and analysis of flame surface density for turbulent premixed combustion on a nozzle-type burner. *Combust. Flame* **122**(1–2), 43–57 (2000)
47. Lindstedt, R., Sakthitharan, V.: Modelling of transient compressible turbulent reacting flows. *Eight Symposium Turbulence Shear Flows* (1991)
48. Lindstedt, R., Váos, E.: Modeling of premixed turbulent flames with second moment methods. *Combust. Flame* **116**(4), 461–485 (1999)
49. Lipatnikov, A., Chomiak, J.: Turbulent flame speed and thickness: phenomenology, evaluation, and application in multi-dimensional simulations. *Prog. Energy Combust. Sci.* **28**(1), 1–74 (2002)
50. Lipatnikov, A., Chomiak, J.: Molecular transport effects on turbulent flame propagation and structure. *Prog. Energy Combust. Sci.* **31**(1), 1–73 (2005)
51. Mandelbrot, B.B.: On the geometry of homogeneous turbulence, with stress on the fractal dimension of the iso-surfaces of scalars. *J. Fluid Mech.* **72**, 401–416 (1975)
52. Meneveau, C., Poinso, T.: Stretching and quenching of flamelets in premixed turbulent combustion. *Combust. Flame* **86**(4), 311–332 (1991)
53. Müller, U.C., Bollig, M., Peters, N.: Approximations for burning velocities and Markstein numbers for lean hydrocarbon and methanol flames. *Combust. Flame* **108**(3), 349–356 (1997)
54. Muppala, S., Aluri, N., Dinkelacker, F., Leipertz, A.: Development of an algebraic reaction rate closure for the numerical calculation of turbulent premixed methane, ethylene, and propane/air flames for pressures up to 1.0 MPa. *Combust. Flame* **140**, 257–266 (2005)
55. Murayama, M., Takeno, T.: Fractal-like character of flamelets in turbulent premixed combustion. *Symp. Int. Combust.* **22**(1), 551–559 (1989)
56. Peters, N.: *Turbulent combustion*, 1st edn. Cambridge University Press (2000)
57. Pitsch, H.: A consistent level set formulation for Large Eddy Simulation of premixed turbulent combustion. *Combust. Flame* **143**(4), 587–598 (2005)
58. Poinso, T., Veynante, D.: *Theoretical and numerical combustion*, 2nd edn. Edwards (2005)
59. Poinso, T., Veynante, D., Candel, S.: Diagrams of premixed turbulent combustion based on direct simulation. *Symp. Int. Combust.* **23**(1), 613–619 (1991)
60. Richard, S., Colin, O., Vermorel, O., Benkenida, A., Angelberger, C., Veynante, D.: Towards Large Eddy Simulation of combustion in spark ignition engines. *Proc. Combust. Inst.* **31**(2), 3059–3066 (2007)
61. Santavicca, G.L., North, D.A.: The fractal nature of premixed turbulent flames. *Combust. Sci. Technol.* **72**(4), 215–232 (1990)
62. Schumann, U.: Subgrid scale model for finite difference simulations of turbulent flows in plane channels and annuli. *J. Comput. Phys.* **18**, 376–404 (1975)
63. Schwertfelm, F., Manhart, M.: DNS of passive scalar transport in turbulent channel flow at high Schmidt numbers. *Turbul. Heat Mass Transf.* **5**, 289–292 (2006)
64. Siewert, P.: Flame front characteristics of turbulent lean premixed methane / air flames at high-pressure. Dissertation, ETH Zürich (2007)
65. Smallwood, G., Gülder, Ö., Snelling, D., Deschamps, B., Gökalp, I.: Characterization of flame front surfaces in turbulent premixed methane/Air combustion. *Combust. Flame* **101**(4), 461–470 (1995)
66. Soika, A., Dinkelacker, F., Leipertz, A.: Measurement of the resolved flame structure of turbulent premixed flames with constant reynolds number and varied stoichiometry. In: *Symposium International Combustion*, vol. 27, 785–792. Elsevier (1998)

67. Tangermann, E., Keppeler, R., Pfitzner, M.: Premixed Turbulent Combustion Models for Large Eddy and RANS Simulations. Proceedings of ASME Turbo Expo pp. GT2010–22,298 (2010)
68. Tangermann, E., Pfitzner, M.: Evaluation of combustion models for combustion-induced vortex breakdown. *J. Turbul.* **10**(7) (2009)
69. Vervisch, L., Domingo, P., Lodato, G., Veynante, D.: Scalar energy fluctuations in Large Eddy Simulation of turbulent flames: statistical budgets and mesh quality criterion. *Combust. Flame* **157**(4), 778–789 (2010)
70. Veynante, D., Trouvé, A., Bray, K.N.C., Mantel, T.: Gradient and counter-gradient scalar transport in turbulent premixed flames. *J. Fluid Mech.* **332**, 263–293 (1997)
71. Veynante, D., Vervisch, L.: Turbulent combustion modeling. *Prog. Energy Combust. Sci.* **28**, 193–266 (2002)
72. Wang, G., Boileau, M., Veynante, D.: Implementation of a dynamic thickened flame model for Large Eddy Simulations of turbulent premixed combustion. *Combust. Flame* **158**(11), 2199–2213 (2011)
73. Weller, H., Tabor, G., Gosman, A., Fureby, C.: Application of a flame-wrinkling LES combustion model to a turbulent mixing layer. Twenty-Seventh Symposium on Combustion. Symp. Int. Combust. **27**, 899–907 (1998)
74. Zimont, V., Battaglia, V.: Joint RANS/LES approach to premixed flame modelling in the context of the TFC combustion model. *Flow Turbul. Combust.* **77**, 305–331 (2006)
75. Zimont, V.L.: A numerical model of premixed turbulent combustion of gases. *Chem. Phys. Rep.* **14**(1), 993–1025 (1995)